University of Alberta

Metal Particle Catalyst Formation from Thin Films for the Creation of Vertically Aligned Carbon Nanotube Structures

by

Brian Olsen

A thesis submitted to the Faculty of Graduate Studies and Research
in partial fulfillment of the requirements for the degree of

Master of Science

in

Materials Engineering

Chemical and Materials Engineering

Fall 2011
Edmonton, Alberta

This thesis is dedicated to
My wife, Kathalina.

Abstract

This work contains research associated with the metal catalysts used in the formation of vertically aligned carbon nanotube (VACNT) films through catalytic chemical vapour deposition (CCVD). The solid-state dewetting process of thin metal films is studied using Ni. In the dewetting process, grain growth is followed by hole nucleation and growth at grain boundaries due to thermal grooving and curvature induced surface diffusion respectively. Coarsening continues after the percolation limit due to Ostwald and Smoluchowski ripening. A 2 nm $Cr_{50}Fe_{35}Ni_{15}$ catalyst is found to grow the tallest VACNT films. This catalyst is found to have excellent stability against coarsening. This stability is found to be the result of Cr oxide that forms before the sample enters the CCVD reactor, but does not reduce in the reactor environment. The VACNT film is comprised of multi-walled carbon nanotubes (MWCNT) produced through base growth and whose average diameter is $\sim$12 nm.

Preface

This work will, for the most part, follow the research as it was chronologically performed. This gives the directions and the thoughts as to why the experiments were performed and what the expected results were at the time. Chapter 1 gives an introduction to CNTs in general and the formation of VACNT films. It also covers the importance of the metal catalyst in the formation of both these structures. Chapter 2 reviews the experimental techniques and conditions used to form the metal catalyst and grow CNTs as well as the techniques used to study the samples produced. These techniques include, sputter deposition, catalytic chemical vapour deposition (CCVD), atomic force microscopy (AFM) and transmission electron microscopy. Chapter 3 describes research into the mechanisms of solid-state dewetting of thin films. This process is necessary in the formation of catalyst particles from thin metal films. Chapter 4 describes the design and discovery of effective growth catalysts for use in commercial CVD reactors. Finally, chapter 5 covers the conclusions of this work.

Acknowledgements

I would like to thank Erik Luber for his assistance in this work, including the great work done to help complete the Ni dewetting research, Babak Shalchi for his microscopy skill, as well as my supervisor David Mitlin.

Contents

List of Figures

List of Abbreviations

Abbreviation	Meaning
CNT	Carbon nanotube
SWCNT	Single walled carbon nanotube
MWCNT	Multi-walled carbon nanotube
AFM	Atomic force microscopy
CVD	Chemical vapour deposition
CCVD	Catalytic chemical vapour deposition
VLS	Vapour-liquid-solid
SEM	Scanning electron microscopy
TEM	Transmission electron microscopy
SAD	Selected area diffraction
DRP	Diffraction Ring Profiler
XRD	X-ray diffraction
TRDR	Time resolved differential relectometry
FDTD	Finite-difference time-domain

1

Introduction

1.1 Vertically Aligned Carbon Nanotube Films

The goal of this work is to look at the variables that affect the growth of vertically aligned carbon nanotube (VACNT) films. These types of structures are formed from growing carbon nanotubes (CNTs) in close proximity to one another. The CNTs usually grow in arbitrary directions, but when close together on a flat substrate, the CNTs align parallel due to lateral spacial confinement. This produces a thick film like structure of vertically aligned CNTs. Though this film like growth is self terminating, films have been grown to millimeters in length before the catalyst becomes ineffective [1].

1.2 Carbon Allotropes

CNTs are an allotrope of carbon first discovered in 1991 by Ijima [2]. The most common allotropes of carbon are diamond and graphite. Diamond is optically transparent and can be found in natural carbon deposits that have been exposed to high temperatures and pressures in the earth's crust. The crystal structure is cubic and based on a FCC lattice with a basis of 2. Graphite is the most stable allotrope of carbon at standard conditions. Its structure is based on carbon atoms forming hexagonal rings and packing these rings to form sheets similar to honeycomb. These sheets are then stacked with every other layer offset to form the crystal structure (see figure 1.1(a)). These sheets individually form another allotrope known as graphene (see figure 1.2 background). CNTs can be seen as a rolled up graphene sheet, but they are also related to another carbon allotrope known as a buckminsterfullerene and are classified in the family of allotropes know as fullerenes. The buckminsterfullerene is a closed spherical structure consisting of carbon hexagon and pentagon rings forming a truncated icosahedron as seen in figure 1.1(b) [3]. Sixty carbon atoms are necessary to form the truncated icosahedron giving rise to the shortened designation of C_{60}. Buckminsterfullerenes are named after Richard Buckminister Fuller because of his research into using geodesic domes in architecture. Figure 1.1(c) shows a CNT structured of a C_{60} molecule to show the relation of these fullerene types.

1.2.1 Carbon Nanotubes

CNTs can vary in diameter and structure orientations giving rise to different structural and electrical properties. Even though CNTs are produced in more of an extrusion or grow method, for conceptual reasons, it is easier to imagine different geometries of tubes when starting from a graphene sheet. If one thinks of rolling a sheet of graphene into a tube, as can be done with paper,

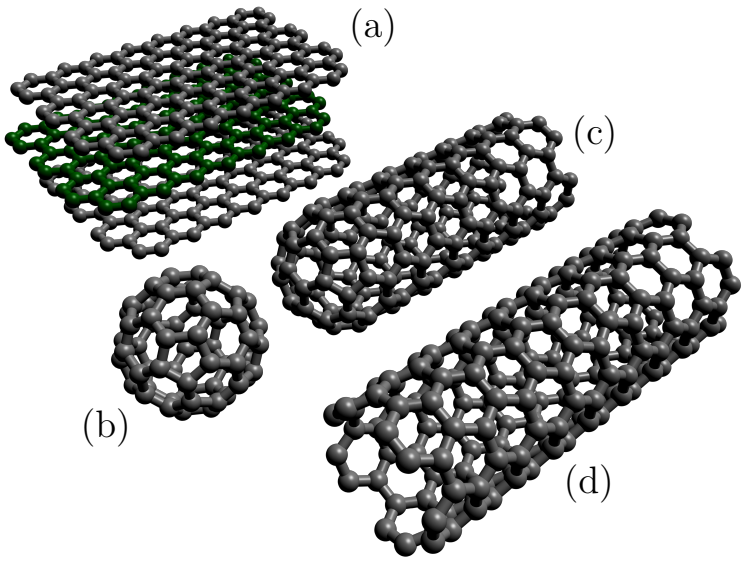

Figure 1.1: A diagram showing carbon allotropes related to CNTs. (a) shows graphite structure with offset layers of hexagonally structured graphene. (b) shows C_{60} buckminsterfullerene. (c) and (d) are closed and open ended CNTs respectively.

there are two different edges that can be joined in the hexagonal lattice. One is a zigzag edge of carbon bonds and the other edge, commonly called armchair, is the shape of a hexagon cut in half at its vertices. An armchair CNT can be thought of as a graphene sheet rolled up and joined at the zigzag edge leaving the armchair edge exposed at the end of the CNT as can be seen in figure 1.1 (d). Similarly, a zigzag CNT would have a zigzag edge at its end. The diameter of the CNT is determined by the number of carbon hexagons in the circumference, or the size of the graphene sheet necessary to form the CNT.

Now imagine taking a sheet of graphene and rolling it to form an armchair CNT, but instead of matching the zigzag edge so the armchair end is square at the end, shift the meeting zigzag edges laterally so the hexagon lattice no longer forms separate rings but a continuous spiral. These types of CNTs no longer have mirror symmetry like the armchair and the zigzag CNTs, but are termed chiral having left and right-handed spiral directions. Figure 1.2 defines nomenclature for CNT structures using the chiral vector $\mathbf{c_h}$ defined as:

$$\mathbf{c_h} = n\mathbf{a_1} + m\mathbf{a_2} \tag{1.2.1}$$

where n and m are two integer indices [4, 5]. The indices are applied to vector directions $\mathbf{a_1}$ and $\mathbf{a_2}$ on the two opposing zigzag directions on the graphene sheet. These indices (n,m) define the CNT structure, for example, an armchair CNT is (n,n) and zigzag (n,0). In figure 1.2, the chiral vector $\mathbf{c_h}$ in that case represents a (2,4) nanotube, which is actually quite small for a nanotube. The CNTs in figure 1.1(c) and (d) are both (5,5) armchair type tubes. The magnitude of the chiral vector $|\mathbf{c_h}|$ is the circumference of the nanotube. Since the angle between $\mathbf{a_1}$ and $\mathbf{a_2}$ is 60°, $\mathbf{a_1} = a\hat{i}$ and $\mathbf{a_2} = a(\frac{1}{2}\hat{i} + \frac{\sqrt{3}}{2}\hat{j})$, therefore:

$$|\mathbf{c_h}| = a\sqrt{\left(n + \frac{m}{2}\right)^2 + \left(\frac{m\sqrt{3}}{2}\right)^2} \tag{1.2.2}$$

$$|\mathbf{c_h}| = a\sqrt{n^2 + nm + m^2} \tag{1.2.3}$$

From this, the diameter of a CNT based on its indices is:

$$d = \frac{a}{\pi}\sqrt{n^2 + nm + m^2} \tag{1.2.4}$$

Where n and m are integer indices and $a \approx 2.5$Å,for a carbon lattice [5].

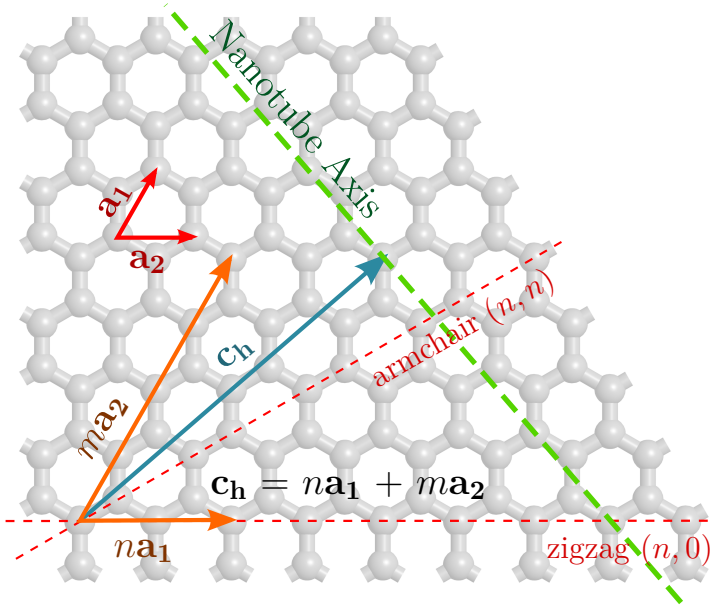

Figure 1.2: A diagram explaining the naming structure of CNTs overlain on a graphene. The chiral vector $\mathbf{c_h}$ is perpendicular to the tube axis and its magnitude is equal to the tube circumference. The chiral vector is defined as $\mathbf{c_h} = n\mathbf{a_1} + m\mathbf{a_2}$ where $\mathbf{a_1}$ and $\mathbf{a_2}$ are vectors corresponding to zigzag directions of graphene as shown and n and m are integers.

The electrical properties of CNTs change with their orientation. Armchair type CNTs always exhibit metallic conductivity while zigzag and chiral tubes have metallic conductivity when $n - m$ is a multiple of three, otherwise they are semiconducting [5].

1.2.2 Multi-Walled Carbon Nanotubes

The CNTs that have been discussed up to this point consist of a single layer of graphene forming a tube. CNTs can also grow with multiple tubes forming concentrically, getting larger in diameter with each layer (see figure 1.3). These tubes are referred to as multi-walled carbon nanotubes (MWCNT). MWCNTs have a similar spacing between their walls as the spacing of graphene sheets in graphite, about 3.4Å. Since the MWCNTs include so many different sizes of tubes, they usually have metallic conductivity [6].

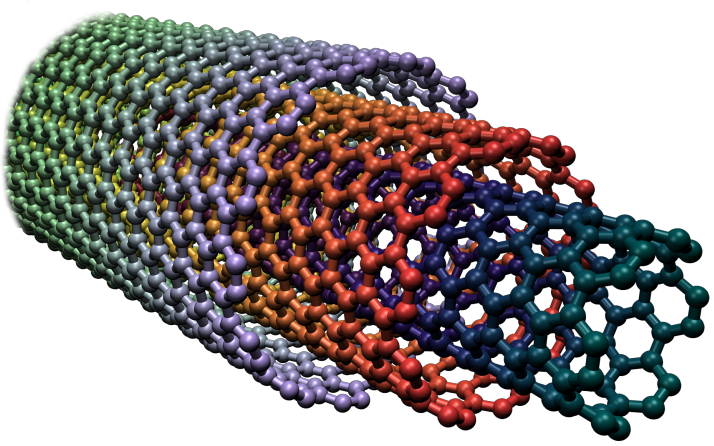

Figure 1.3: False colour representation of a multi-walled carbon nanotube.

1.3 Carbon Nanotube Growth

VACNT films are usually grown in a catalytic chemical vapour deposition (CCVD) process with acetylene (C_2H_2), ethylene (C_2H_4) or carbon monoxide (CO) as common carbon source gases. Metal catalyst particles, usually Fe, Ni, or Co, are applied to a flat substrate. When placed at high temperatures with

the carbon source gas, the catalyst becomes a template for the CNT growth. Depending on the temperature of the process and the particle substrate interaction, the catalyst will either adhere to the substrate and the tube is said to have base growth, or if the interaction is weak, then the CNT may grow under the catalyst and the catalyst will be at its tip, in tip growth (see figure 1.4).

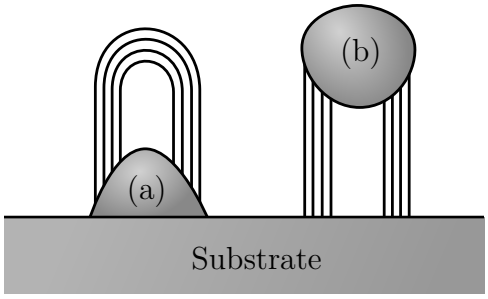

Figure 1.4: A diagram of the two basic growth modes found in CNTs, (a) base growth and (b) tip growth

1.3.1 Carbon Nanotube Growth Mechanism

As previously discussed, CNT growth resembles an extrusion of cylindrical tubes of graphene from the catalyst particles. This type of CCVD growth was first seen in the growth of silicon whiskers in the 1960's. At that time, Wagner and Ellis [7] proposed the vapour-liquid-solid (VLS) mechanism to explain the growth of these whiskers. The VLS mechanism involves three steps: first, the growth element containing gas is dissolved into a liquid catalyst particle; next, the growth element diffuses through the catalyst to the growth front; finally, the growth element forms into a solid crystal structure(see figure 1.5). This VLS mechanism was extended to growing carbon fibres in the 1970's by Baker *et al.* [8] and then more recently to CNT growth by Kanzow *et al.* [9]. Kanzow *et al.* proposed that the VLS model could also be extended to solid catalytic particles seen on low temperature CCVD (600-900°C) where solid state diffusion of the carbon could occur in the catalyst. This mechanism relies

on a temperature gradient to drive diffusion of carbon from the areas heated by exothermic dissociation of the feed gas to the wall growth sites where it is cooler since dissociation cannot occur. Resent simulations of small catalyst particles growing single walled CNTs (SWCNTs) show that the temperature gradient has little effect and that the diffusion is dominated by consecration gradients where the concentration is less at the growth points [10].

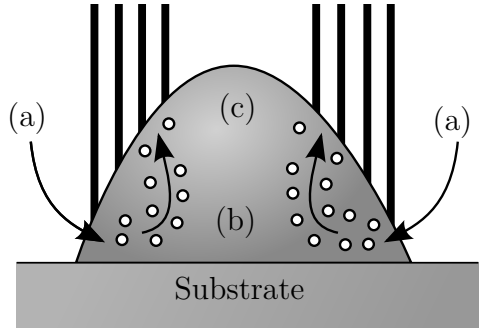

Figure 1.5: A diagram of the vapour-liquid-solid (VLS) growth model in carbon nanotubes. (a) The carbon source gas disassociates on the surface of the particle with the carbon going into solution. (b) The carbon in solution diffuses to CNT wall nucleation point via a temperature gradient. (c) The carbon forms bonds with the wall of the tube that extend the structure from the base.

Figure 1.6 shows the formation and growth of MWCNTs on a catalyst particle. The particle first becomes super saturated with carbon when exposed to carbon source gas and some carbon atoms start to form bonds with each other on the particle surface. The carbon atoms bind to each other on the particle surface and then detach from the particle to form a half fullerene-like structure which defines wall of the carbon nanotube [11]. If the particle is sufficiently large, multiple fullerene domes can form becoming the basis for the multiple walls in a MWCNT, otherwise a SWCNT will form. The walls continue to form by having carbon from the particle fill in the atom sites in the graphene walls [12].

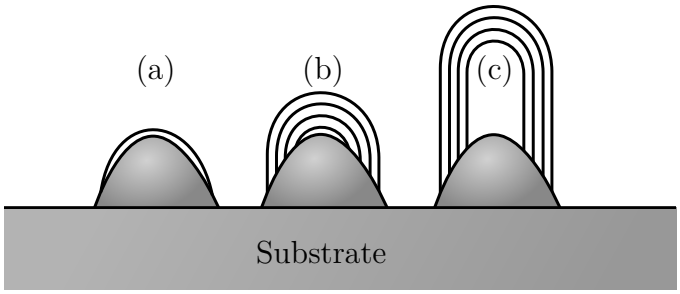

Figure 1.6: A diagram showing the formation and growth of a MWCNT under the VSL growth model. (a) A stable fullerene-like cap of carbon forms on the particle surface and detaches. (b) Additional smaller caps form and CNT walls start to form near the particle edge. (c) The wall continues to form with stable graphite-like basal plane spacing.

CNT growth can be stopped by simply removing the carbon source gas from the reaction furnace, however even if the source gas is not removed the growth will still eventually terminate. The length of a CNT is limited by the amount of carbon diffusing into the catalyst from the feedstock gas and morphological stability of the particles. The catalyst can become poisoned by amorphous carbon buildup on its dissociative surfaces. This buildup prevents the catalyst from incorporating carbon into itself starving the tube growth. Since the CNTs are more stable than the amorphous carbon, the buildup can be burned off by having an oxidizing environment in the reaction chamber during growth [1]. Even without buildup, the growth can still terminate since the particles under go morphological changes during growth at high temperatures [13–15]. Parts of the catalyst can be lost into the CNT or some particles may grow or shrink in size due to particle coarsening and be unable to continue the growth of their supported tube.

1.3.2 Catalyst Properties

The role of the catalyst in the CCVD production of carbon nanotubes is two fold: it is a template for size and distribution of the nanotubes [16, 17]; and it has high carbon solubility or forms a weak carbide to dissociate the carbon carriers below its decomposition temperature or at a faster rate and allows reassociation of the carbon as walls of the CNTs. The particle's size determines the diameter of the CNT as well as the number of walls. To grow CNTs, it is best if the particles are less than 100 nm since the diffusion length in larger particles is too long to adequately supply carbon for nanotube growth. These large particles tend to make flat layers of graphite or amorphous carbon instead of CNTs [18]. The distribution of the active catalyst is important in the morphology of the overall film. If the density of active catalytic sites is low, the CNTs grow in random directions forming an intertwined jungle-like structure of long tubes that wind across the substrate. With a high density, the CNTs are constrained laterally and the only favourable growth direction is vertically away from the substrate. These vertical growing tubes are still quite wavy and intertwined, but the general growth direction of the tubes is upwards. This vertically aligned CNT (VACNT) growth can form dense film-like structures of CNTs that can be microns tall (see figure 1.7). Care must be taken in selecting a substrate that is not reactive with or has solubility for the catalyst metal used. Often substrates such as SiO_2 or Al_2O_3 are used because of their stability at high temperatures.

The other role of the catalyst is to preferentially dissociate the carbon carriers in the CCVD reactor. The catalyst can either affect the feed gas decomposition thermodynamically by allowing a reaction pathway that would decompose the gas at a lower temperature than normal, or kinetically by allowing a faster pathway for the decomposition so the catalyst particles disassociate the feed gas many times faster than the substrate. In this way, the CNTs have time to grow before the catalyst is poisoned by the build up of amorphous carbon on

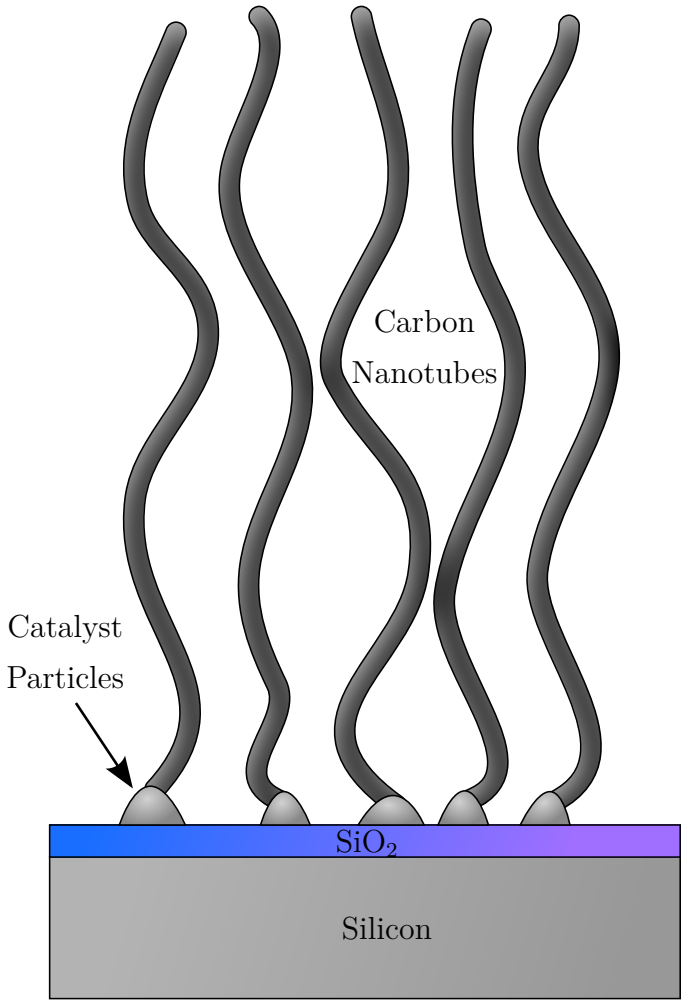

Figure 1.7: A diagram of a VACNT film showing how the density of active catalytic sites leads to vertical growth.

the substrate and catalyst particles.

1.3.3 Catalyst Production

In CCVD production of carbon nanotubes, metallic particles are applied to a substrate using several different techniques. Nanoparticles produced in solution can be applied to substrates as catalysts. These particles can be produced with a low variance in size, but they are difficult to produce and to distribute evenly on the substrates. Chemical deposition of metal catalyst from metal containing salts give an even distribution, but varying sizes. The metal catalyst can be applied in the CVD reactor as well, either through an oxide reduction or from a vaporized metal containing solution such as ferrocene [19]. Physical Vapour Deposition techniques such as evaporation or sputtering can be used to deposit metal catalyst as a film. This film when heated in the CVD reactor undergoes a process known as solid-state dewetting where the film breaks up to form catalyst particles. This process is easy, scalable, and provides an excellent spacial density of particles capable of growing VACNT films, but it is difficult to tune the size and the size distribution of the particles. This technique of dewetting catalyst will be treated extensively in chapter 3.

2

Experimental Techniques

In this study, several techniques were used to synthesize and characterize CNT growth. Sputtering was used to deposit CNT catalyst and CCVD was used to dewet the catalyst and grow the CNTs. Atomic force microscopy (AFM) was used to characterize the dewetting properties of the catalyst. Transmission electron microscopy (TEM) was used in characterizing the catalyst as well as the CNTs.

2.1 Sputtering

This project uses DC-magnetron confocal co-sputtering to produce catalysts for CNT growth at different alloy compositions. The sputtering is performed in vacuum systems with low pressure (mTorr) of inert gas (usually argon). Sputtering was first done between two parallel plates with a large electric potential applied across them. The cathode is the target that contains the material to be deposited and the anode is the substrate where the deposition occurs. Under the potential, loose electrons can collide with the inert argon in the chamber. If the collision is strong enough, an electron is ejected and the Ar become ionized Ar^+. The Ar^+ is accelerated towards the target. When argon collides with the cathode, secondary electrons are released which can be used to ionize more argon atoms. This sets up a cascading effect where a high energy plasma is produced between the two plates. If the Ar^+ ions collide with the target with enough energy, then atoms from the target element can be sputtered. Sputtering is when an atom is ejected from the target as a result of a domino effect of colliding atoms in the target initiated from an argon collision. If the ballistic trajectories of the colliding atoms in the target are properly alined, then the sputtered atoms travel from the target to the substrate without the need to be charged. The characteristic glow of the plasma results from argon electron collision where the energy is insufficient to ionize the argon, but the argon electrons are moved to a more excited state. When the excited electrons fall to their base state, a photon is emitted.

Modern sputter equipment uses magnetic confinement in the form of magnetrons to increase electron density at the target. A magnetron produces closed loop magnetic field lines that run over the target. The electrons in the system are trapped in orbits around these field lines and the density of electrons is increased near the target. This allows for a lower argon pressure to form a plasma since the number of argon-electron collisions near the target are increased. Having lower argon pressures increase the mean free path of

the sputtered flux from the gun allowing for usable rates at greater distances between the target and substrate. The rate of deposition is also increased in magnetron sputtering since the number of Ar^+ ions is increased. With magnetically confined electrons, it is no longer necessary to have the parallel plate to induce the plasma, but a gun configuration can be used. In the gun configuration, the anode is a ring around the target (cathode) and the secondary electron are attracted to the ring but become caught in the magnetic field instead. The sputtered material follows a ballistic trajectory from the gun to the substrate unaffected by the magnetic field since it is uncharged. The gun configuration allows for multiple guns to be confocally directed at the same substrate to allow different element to be sputter simultaneously or co-sputtered (see figure 2.1).

2.1.1 Co-Sputtering Alloy Compositions

To deposit different alloy compositions through co-sputtering, the rates of the deposition can be varied by adjusting the relative gun powers. The deposition times must be equal to have the same composition throughout the film thickness. Substrate rotation is necessary to ensure that the incident flux evenly coats the surface. The rates of the sputtered materials can be measured for a given power through a deposition monitor on the system. The deposition monitor is placed in the sputter flux at the hieght of the substrate. The monitor contains a piezoelectric crystal that is resonated at high frequency (Mhz). The monitor detects small changes in this frequency due to the additional deposited mass from the sputtered flux. If the material's density is known, the thickness of deposited material and thus the rate of deposition can be calculated. The atomic composition x in A_xB_{x-1} is calculated from:

$$x = \frac{R_A\rho_A}{R_A\rho_A + R_B\rho_B} \tag{2.1.1}$$

where R_A and R_B are the deposition rates and ρ_A and ρ_B are the molar

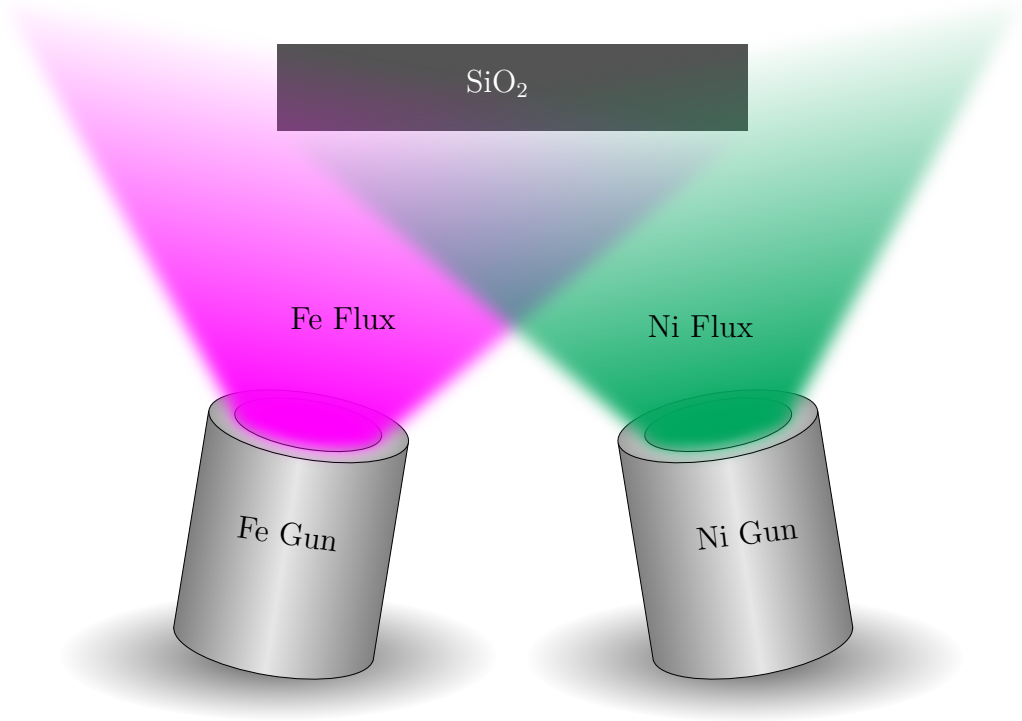

Figure 2.1: A diagram showing the overlapping flux from two magnetron sputter guns during confocal co-sputtered deposition. This particularly shows the situation of Fe and Ni co-sputtered deposition onto SiO_2 used in this study

densities of the element A and B. To design an alloy of composition of x and a measured R_B, R_A must be adjusted according to:

$$R_A = \frac{R_B \rho_B}{\rho_A} \frac{1}{1-x} \tag{2.1.2}$$

Assuming a linear relation between gun power and deposition rate like $R(P) = aP + b$. Where a and b are solved by fitting a line to measured rates. This gives the power necessary to produce composition x as:

$$P_A = \frac{R_B \rho_B}{a \rho_A} \frac{1}{1-x} - \frac{b}{a} \tag{2.1.3}$$

Assuming that the alloy's final density will be close to the simple addition of the original elemental densities, then the total film height should be approximately:

$$h_{AB} \approx (R_A + R_B)t \tag{2.1.4}$$

2.1.2 Sputtering Experimental Conditions

In this study, sputter deposition (AJA International, Orion 8) was used to produce all single element, binary, ternary, and multilayer catalysts used to grow CNTs in the CCVD process. The base pressures of the vacuum system were below 3×10^{-8} Torr for all depositions. As the catalyst films were quite thin (lest than 5 nm), the deposition rates were kept low to ensure even deposition coverage via substrate rotation. The substrates used in this study were oxidized silicon wafers, with oxide thickness greater than 100 nm to prevent reactions with the Si at the temperatures used in the CCVD reaction.

2.2 Catalytic Chemical Vapour Deposition

Chemical vapour deposition is any process in which gaseous chemical precursors react in a chamber resulting in a deposition. This process can be done at different temperatures and pressures to vary the reaction conditions. In some cases, plasma or combustion is used to assist in the reaction. A catalyst is used to assist in the reaction process to increase the reaction rate. Since the rate of the reaction is greatest on or near the catalyst, the areas of deposition on the substrate can be selected through patterning the catalyst.

In producing CNTs through CCVD, elevated temperatures are used and the reaction is usually a simple decomposition of carbon containing gases. The catalyst aids in the decomposition by having high carbon solubility. The catalyst offers a pattern on the substrate that affects the shape of the CNTs that are formed (see chapter 1).

2.2.1 CCVD Experimental Conditions

The CCVD reactions in this study were performed in a tube furnace CVD reactor (Tystar Inc.) capable of processing 50, 150 mm wafers in a run. The oxidized silicon substrates with catalyst were placed into the tube furnace at 550°C and then ramped to 750°C in a 3000 sccm flow of 10% hydrogen in argon at 10°C min^{-1}. To allow the catalyst films to dewet into particles, the samples were then annealed in the same environment for 35 minutes at 750°C. The hydrogen was added to reduce the natural oxides that form on the catalyst metals after removal from the sputter deposition system. Growth of the CNT was performed for 5 minutes at 750°C in 15% ethylene and 10% hydrogen in argon (total flow 3300 sccm). The samples were then cooled to below 450°C before removal from the tube furnace.

2.3 Atomic Force Microscopy

Atomic force microscopy (AFM) is a type of scanning probe microscopy that was developed by Binning *et al.* [20] in 1986 at IBM research shortly after the development scanning tunnelling microscopy. The technique involves scanning a sharp tip on the end of a cantilever over the surface of a sample and measuring the deflection of the cantilever as the tip interacts with the surface(see figure 2.2).

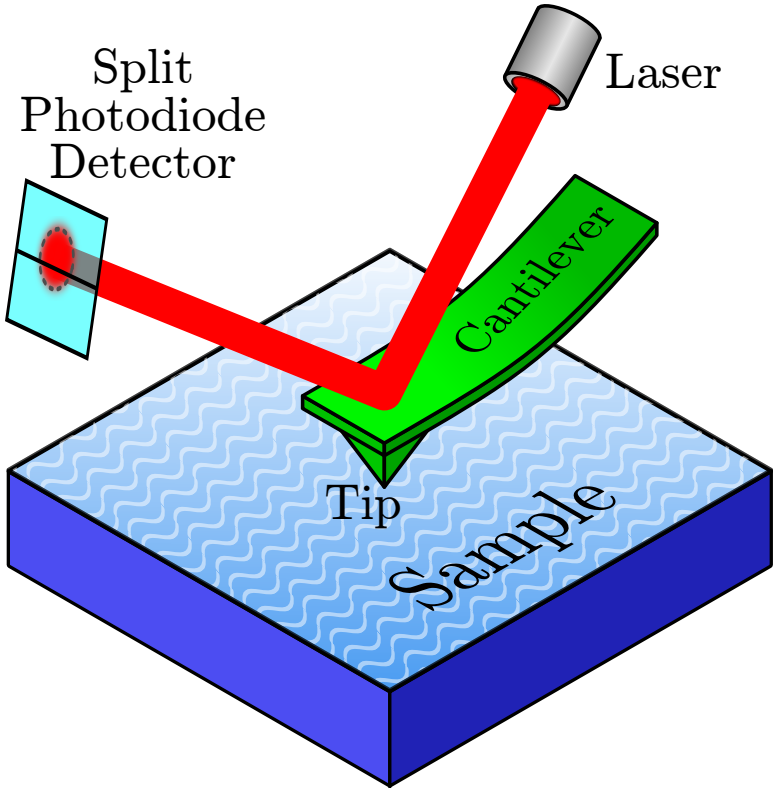

Figure 2.2: A simplified schematic of an atomic force microscopy (AFM) setup showing a laser reflecting off a tipped cantilever to a split photodiode detector. As the tip interacts with the sample surface, the cantilever deflects and the resulting change in laser direction is detected on the photodiode.

The deflection of the tip is measured by a laser that is reflected off the cantilever and onto a split photodiode detector. The split photodiode consists of a pair

of photodiodes meeting edge to edge in the detector's center. When the laser is centered on the detector, the voltages measured on both photodiodes are equal. The laser's reflection and therefore the cantilever deflection, is measured by comparing the relative voltages across the photodiodes in the detector. In order for the detector to know the location of the spot to calculate the cantilever's deflection, a voltage greater than zero must be measured on both photodiodes. A four section split photodiode is often used to measure twisting of the cantilever due to lateral tip-sample interactions.

The motion of the tip across the surface is enabled by a piezoelectric stage. Either the tip or the sample is mounted to the motion stage to enable the tip to move relative to the sample. The stage is usually a four section cylinder of piezoelectric material, which allows motion in all 3 dimensions. Voltage can be applied to this cylinder to scan the sample under the tip, where each scan line is slightly offset so a mapping of the sample surface is formed. The piezoelectric movers can be precise enough to achieve atomic resolution scans. The height map is usually produced by changing the height of the scanning stage in a feed back loop with the split photodiode detector where the stage changes height to keep the deflection of the cantilever constant.

The sharpness of the tip determines the smallest lateral dimensions of features detectable on the surface. If the peaks of the sample are spaced closer together than the radius of the imaging tip, then the tip will be unable to probe between the highest features and the sample will appear flat. Regardless of the sharpness of the tip the features on the AFM height map are always dilated laterally by the size of the tip. To reduce these affects, one should use as sharp a tip as available, but sharp tips wear more quickly as the tip is scanned across the surface.

To reduce the wear on the tips and therefore allow scanning with even sharper tips, the AFM can be use in tapping mode. Previously, the cantilever was kept at a constant deflection throughout scanning. This mode is called con-

tact mode since the tip is always in contact with the surface when the cantilever is deflected. In tapping mode, the cantilever is vibrated at a frequency near its resonance by a piezoelectric element. The amplitude of the cantilever's oscillations is measured by the split photodiode detector. The change in amplitude as the tip scans is used in feed back with the scanning stage to determine the sample height.

2.3.1 AFM Experimental Conditions

In this study, a Veeco (now Bruker AXS) MultiMode AFM was used in tapping mode under ambient conditions. Tips (AppNano ACTA) with radius of curvature of 6 nm were used for the samples with large features. For samples with smaller features, tips (AppNano ACTA-SS) with a radius of 2 nm were used with a more sensitive piezoelectric scanning stage.

2.4 Transmission Electron Microscopy

In transmission electron microscopy, a beam of electrons is focused on a small area of a sample and the electrons that pass through the sample are analyzed. The electrons that pass through the sample are then magnified by magnetic lenses and can be projected to form an image of the sample on a phosphor screen. Contrast in the image formed can be a result of variance in electron absorption from either differences in thickness or Z number of the sample or a result of diffraction from crystal structures. By placing an aperture in the center of the back focal plane, an image can be formed with only absorption contrast. Such an image is called a bright-field image.

If the focal back plane is projected onto the phosphor screen, a pattern is produced that indicates the electron diffraction that occurred in the sample.

Usually an aperture is used so the diffraction pattern is only from the area corresponding to the aperture. This is called selected area diffraction (SAD). A SAD from a single crystal forms a pattern of spots based on the symmetry, spacing, and orientation of the crystal planes in the sample according to Bragg's law:

$$n\lambda = 2dsin(\theta) \tag{2.4.1}$$

where n is an integer, lambda is the de Broglie wavelength of the electrons, d is the distance between the diffracting planes and theta is the angle between the incident electrons and the crystal plane. In a poly-crystalline section of sample, sharp rings are formed as the diffraction pattern. With random crystal orientation, the rings represent all the possible plane spacings in the crystal structure of the material. The rings form because of the many different rotational orientations around the electron beam that satisfy the Bragg condition. The diffraction pattern of amorphous materials appear as broad rings or halos whose spacing are based on nearest neighbour distances of the atoms.

2.4.1 TEM Experimental Conditions

TEM in this study was performed, in a Japan Electron Optics Laboratory (JEOL) 2100 microscope with an electron accelerating voltage of 200kV. The samples were prepared on 20 nm thick amorphous SiO_2 windows from SiMPore Inc. to ensure a similar substrate interaction as the other samples.

2.4.2 Diffraction Ring Profiler

Since the amount of catalyst used in this study was too little to get meaningful X-ray diffraction results, rigorous evaluation of SAD ring patterns was performed. To aid in evaluating these ring patterns, a software program known

as Diffraction Ring Profiler (DRP) was made.

DRP allows a ring pattern image to be converted into a profile showing the intensities and spacings on a graph that looks similar to X-ray diffraction patterns from a linear detector. The program takes in a digital image file from the microscope CCD or scanned film, and gives tools to the user to calibrate and find the approximate center of the pattern. The center approximation and calibration is implemented by having the user select three points on a ring, which allows for the center and the radius of the ring to be uniquely defined(see figure 2.3).

Calibration is done on a sample with known plane spacings to determine the resolution of the CCD image from the camera length given by the TEM apparatus. If the pattern is from digitally scanned film, then the resolution of the image is the scanned resolution in pixels per inch. As seen in figure 2.4, the camera length given by the TEM apparatus is defining the effect of the magnification applied to the diffraction pattern. The pattern resultant from the magnification is the same physical size as one produced by an apparatus with no magnification and with a sample to detector distance equal to the given camera length. From figure 2.4 it can be said:

$$\tan(2\theta) = \frac{r}{L} \tag{2.4.2}$$

where L is the camera length, r is the radius of the diffraction ring and 2θ is the angle between the diffracted beam and the beam axis. θ is the angle satisfying the Bragg condition for diffraction. In TEM $\theta \ll 1$, so the small angle approximation of $\tan(2\theta) = 2\theta$ gives:

$$2\theta = \frac{r}{L} \tag{2.4.3}$$

Also applying the small angle approximation of $\sin(\theta) = \theta$ in Bragg's Law (equation 2.4.1) gives:

$$\lambda = 2d\theta \tag{2.4.4}$$

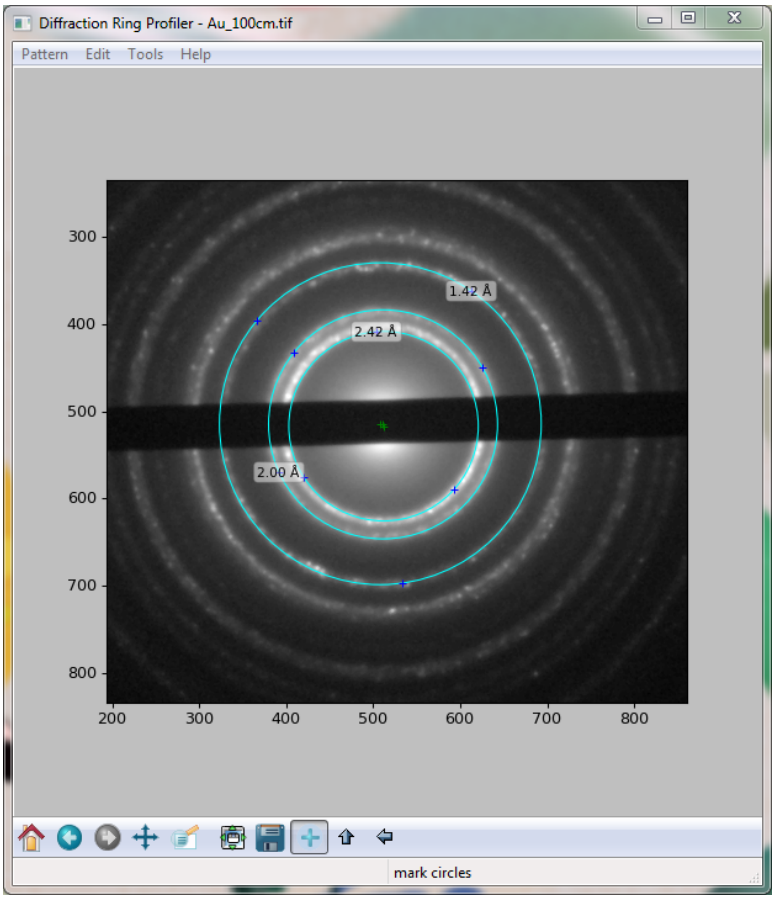

Figure 2.3: A screenshot of Diffraction Ring Profiler (DRP) showing used defined 3-point circles and the calibrated d-spacings. The pattern in the screenshot is that of Au at 100 cm camera length, a typical calibration sample.

To solve for the spacings of the crystal plane of d-spacings in term of r and L we apply equation 2.4.3 to equation 2.4.4 to get:

$$d = \frac{\lambda L}{r} \tag{2.4.5}$$

where for electrons λ is the de Broglie wavelength, which can be found from the accelerating voltage applied to the electrons with:

$$\lambda = \frac{h}{\sqrt{2m_e e V_{acc}}} \tag{2.4.6}$$

where h is Planck's constant, m_e is the mass of an electron, e is the charge of an electron, and V_{acc} is the accelerating voltage. Since the r value for a digital diffraction pattern is in pixels, the image resolution is used to convert the pixels to the same units of L (usually cm).

Once the pattern is calibrated and the center is found, a profile is made from the pattern. The distance of each pixel in the pattern to the center is calculated. These distances are then binned in a histogram that is weighted by the intensity of the pixels themselves. This profile is then used to refine the pattern center by changing the pattern center and optimizing for the sharpest peaks. After the redefined center is found, a polar transform of the diffraction pattern is made to linearize the ring pattern. A new profile is made from this polar pattern. The new profile and the linear pattern are overlaid to compare the ring pattern to its profile. A simulation of the rings can also be applied to the figure so the spacings and the intensity can be easily compared. The inelastic scattering of electrons passing through the sample creates a background signal that can removed from the profile. Figure 2.5 shows a screen shot of a finished figure showing a Au diffraction pattern with a camera length of 100 cm.

Profiles of SAD ring patterns are an excellent way to compare d-spacings and intensity with simulations and other diffraction patterns. As profiles, different patterns can be easily compared one above the other or overlaid on the same

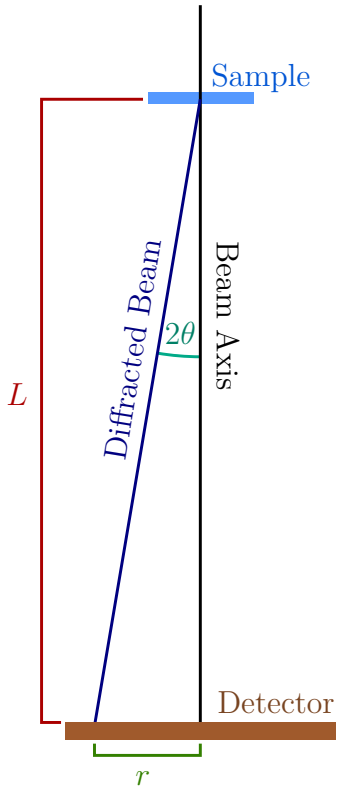

Figure 2.4: A diagram showing the definition of camera length (L). 2θ is the angle between the diffracted beam and beam axis which is in the center of the pattern and θ is the angle satisfying the Bragg condition for diffraction. r is the measured distance from the pattern center to the diffraction ring.

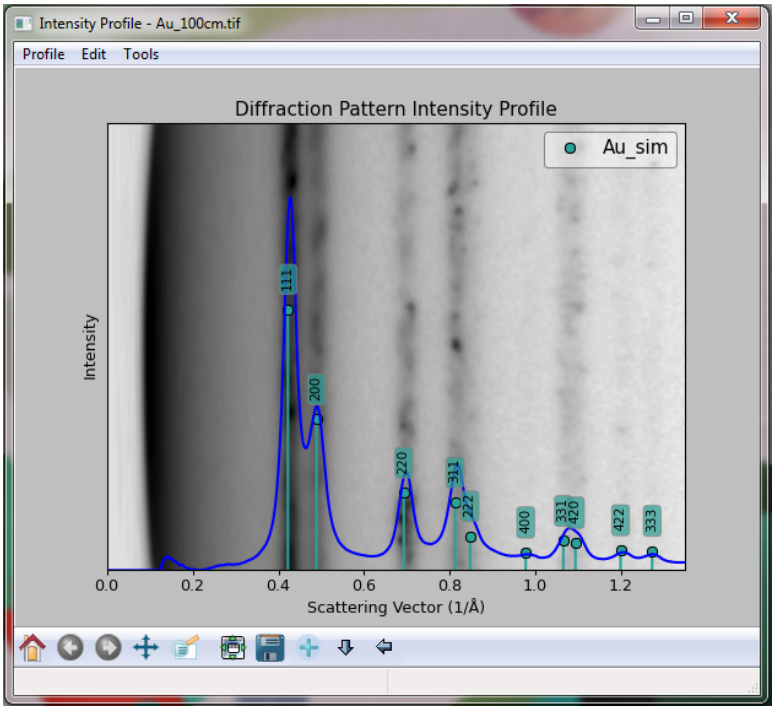

Figure 2.5: A screenshot of DRP's profile window showing a polar pattern of Au with overlain background subtracted profile. Au simulated ring pattern with intensities and indexed peaks is also shown.

graph even if they have different camera lengths. Multiple simulations can also be easily visualized on a profile graph even with overlapping peaks between the phases since the greater intensity of overlapping peaks can be seen.

In figure 2.6, an electron diffraction ring pattern of a 2 nm Ni film, dewet in the sputter system after deposition, is shown as a profile by the green circles. The polar transform of the ring pattern is shown in the background. This pattern was used to calibrate the resolution of the detector using the known d-spacings of Ni. The spacings of peak fit nicely to the simulation. This calibration was used with the other diffraction pattern profiles seen in chapter 4. To see the profile peaks more clearly the background from inelastic scattering and from the amorphous SiO_2 was removed. This particular sample shows oxidization upon removal from the sputter deposition system. Through peak fitting software (Fityk [21]) peaks of the Ni and the NiO are shown in corresponding colours to the simulations. The match of the peak fitting is quite good as shown by there red line. The blue line is used to fit remaining SiO_2 signal. The broadness of the NiO peaks indicate very small crystal grains such as ones formed on the particles surface due to exposure to air upon removal from the deposition system.

Compiled binaries and source code of Diffraction Ring Profiler 1.3 are available online at:

▶ http://code.google.com/p/diffraction-ring-profiler/

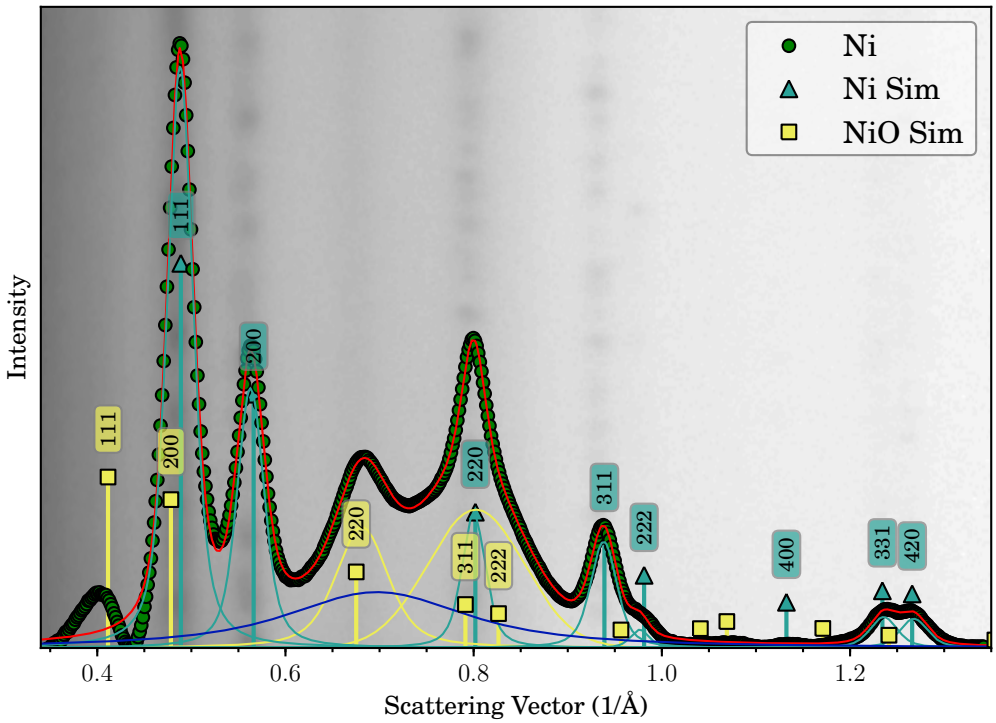

Figure 2.6: A profile of an electron diffraction ring pattern from a 2 nm Ni film dewet *in situ* after deposition (green circles). The solid lines represent peak fitting where the red line is the resultant fit and the other lines correspond to the colour of the peak markers from the diffraction simulation.

3

Ni Dewetting [1] [2]

3.1 Motivation

As mentioned in chapter 1, dewetting is the mechanism of catalyst particle formation from sputter deposited metal films. Since the catalyst particle shape and size determine the characteristics of the resulting nanotubes, a set of dewetting experiments were developed as part of the CNT catalyst study. What started out as a process to replicate experiments by other groups [22–24] by dewetting Ni then extending it to other CNT catalyst metals, ended up

[1] Material in this chapter has been published in:

▶ E. J. Luber, B. C. Olsen, C. Ophus, and D. Mitlin. Phys. Rev. B, 82(8):085407, 2010.

[2] The finite-difference time-domain modelling was performed by E. J. Luber.

with the development of a new *in situ* dewetting measurement technique for dewetting that opens new insights into the relatively unknown mechanisms involved in the solid state dewetting process. These experiments from this novel approach yielded such interesting results they warranted publication on their own.

3.2 Dewetting

The term dewetting refers to the process of a film of liquid on a surface forming droplets because of a drive to reduce its surface free energy as well as the energy of the liquid surface interface. If strong bonds exist between the surface and liquid, the liquid may have a lower energy by wetting the surface. The droplet distribution of a dewetting liquid is determined by the Rayleigh instability which is based on surface free energies.

3.2.1 Solid-State Dewetting

Solid-state dewetting yields similar results to liquid dewetting but the mechanisms are different. In the solid state, the mobility of the atoms is much slower, and therefore the process takes much longer. Most of the atom mobility arises from surface diffusion at elevated temperatures. In a single crystal and likely in amorphous material as well, solid-state dewetting is still governed by Rayleigh instabilities and surface energies [25]. However, most metals form polycrystalline solids. Surface diffusion still dominates atomic transport in polycrystalline metals, but grain boundaries dictate the final distribution.

3.2.2 Thermal Grooving

In polycrystalline solids the holes to start the dewetting process nucleate from thermal grooving at the grain boundaries [26]. As explained by W. W. Mullins [27], thermal grooving is a surface reconstruction process that is driven by the surface wanting a constant curvature, but is pined by an equilibrium dihedral angle at the grain boundary. As the temperature increases, the equilibrium dihedral angle sharpens to allow the groove to deepen. If the film is thin enough or, conversely, the temperature is high enough, a hole will nucleate in the film and dewetting will begin, unless the metal bonds to the substrate. These holes continue to grow and coalesce until the film appears as islands of metal forming particles on the substrate surface.

3.3 Introduction to Reflectometry

While trying to measure stress of Ni films on SiO_2 substrates during deposition and annealing, the *in situ* stress measuring optics on the sputter system were unable to detect the full intensity range of the laser reflection. Surprisingly, the laser intensity went *below* the detectable limit soon after the beginning of the Ni deposition. After running optical simulations using a characteristic matrix approach [28], it was found that, for the laser and optical geometry used, the oxide thickness was near but just thicker than one that would have the highest interference condition for a SiO_2 film on Si upon reflection(see figure 3.1). This thin film interference is caused by path length difference and phase changes between the light reflected off the SiO_2 versus the Si reflection. Since the reflectivity of the SiO_2 is lower, for the laser wavelength, than that of the Si, the system cannot reach a perfect interference condition. Adding a Ni film to the simulation caused the intensity to drop, which explains what was seen during stress measurements. This drop was caused by the increased

reflectivity of the Ni compared to that of the SiO_2 surface. As the reflectivity of the Ni increased upon deposition, the amount of light reaching the Si surface decreased and therefore the Si reflection decreased. Since the two reflections were still out of phase, when their intensities match, they destructively interfered almost perfectly. The intensity dynamics during the anneal step also varied like the deposition, which lead to the idea of tracking this reflectivity for further analysis.

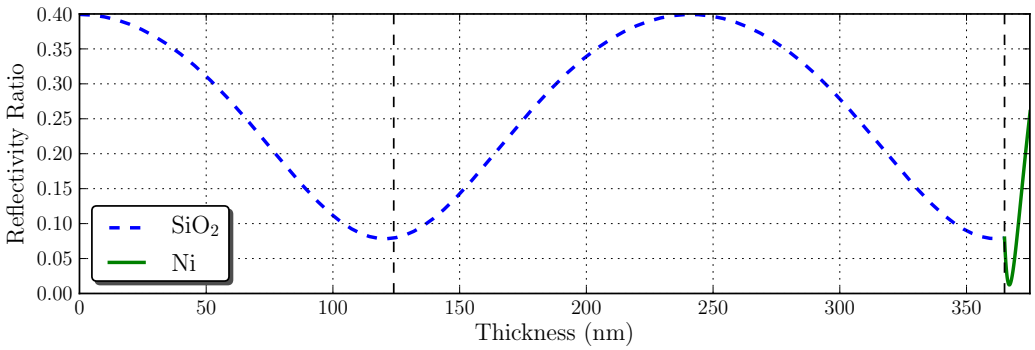

Figure 3.1: A plot of TRDR simulation showing the reflectivity of SiO_2 on Si as the thickness increases. The dotted lines indicate the thicknesses of the two oxide thicknesses used in this study, 124 nm and 365 nm. The affect of Ni deposition on a 365 nm SiO_2 sample is also shown.

3.4 Experimental Procedure

The first oxidized silicon wafer used was just thicker than the second interference condition for the optical setup (365 nm). For later experiments, another wafer was used which was just thicker than the first interference condition (124 nm). Since the optical consistency in the oxide was necessary, the wafers were checked for thickness uniformity and then parted into small pieces. The thickness uniformity of the wafer and later, the thickness of each piece was

measured using a F50 spectral reflectance automated thickness mapper (Filmetrics Inc). The thickness of pieces used in this study were found to be within ±1 nm of each other. These pieces were stored under vacuum (1×10^{-7} Torr) and then used throughout the set of experiments.

It was found early on, by comparing the laser results, that the sputtering base pressure had an affect on the dewetting behaviour of Ni. It was assumed that the water vapour in the sputter system formed an oxide in the Ni film which inhibited grain boundary motion and atom diffusion. To reduce the water vapour in the sputter system, the samples were baked for 2 hours at 500°C, cooled overnight and sputtered at base pressures less than 9×10^{-10} Torr. Also, high purity argon gas (6.0 or 99.9999% pure) was used to prevent oxidization. Ni was deposited at 100 W giving a measured deposition rate of 0.62 Å s^{-1}. After Ni deposition, the samples were ramped to 500°C at a set rate and annealed for 2 hours. The samples were then cooled before removal from the sputter system.

The laser reflectivity was monitored throughout the baking, deposition, annealing, and cooling. The 16 mW 660 nm s-polarized AlGaInP diode laser was mounted at 30° to the substrate normal (see figure 3.2). The detector, a silicon photodiode light meter(ILT 1700), was mounted at 30° in the opposite direction to receive the reflected beam.

Differential reflectivity curves are used in this study to easily compare simulation to experiment or within experiments where other incident laser intensities are used. The differential reflectivity is calculated from the measured reflected intensity by:

$$\frac{\Delta R}{R} = \frac{R - R_0}{R_0} \tag{3.4.1}$$

Where R is the measured reflected intensity and R_0 is the initial measured reflected intensity of the clean SiO_2 sample.

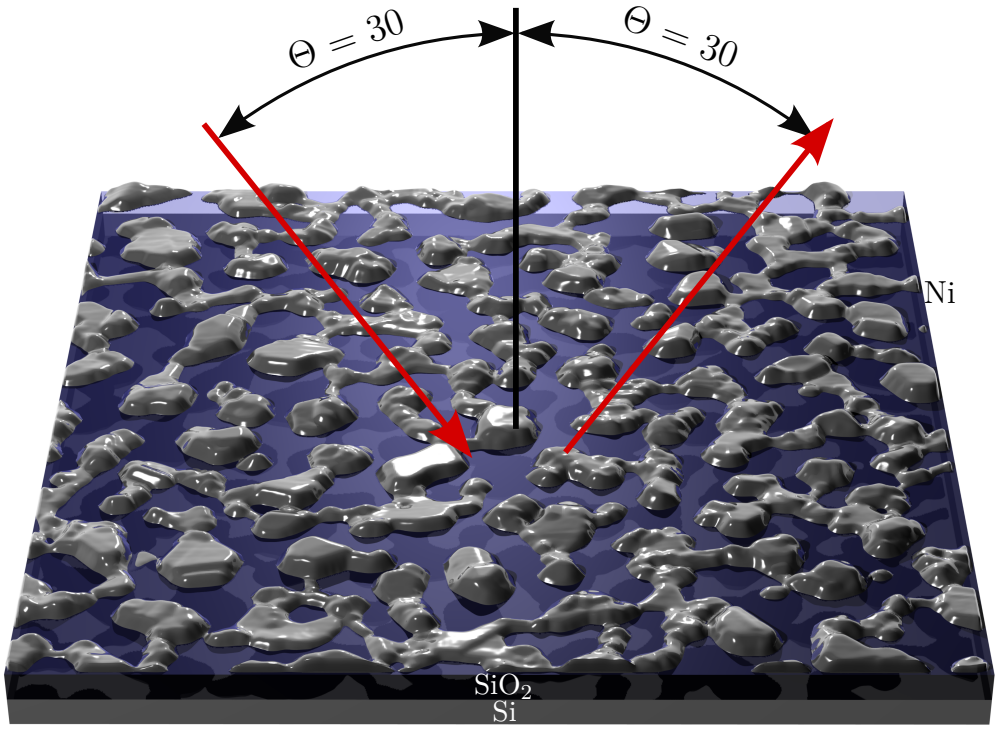

Figure 3.2: A diagram of laser orientation to the substrate. The AFM data used for the background is from a partially dewet 7.5 nm nickel film.

3.5 Time Resolved Differential Reflectometry

3.5.1 During Deposition

Using a light meter to measure the laser reflection intensity, it was found that, during deposition, the first few nanometres of Ni caused the intensity to decrease and then begin to increase as expected upon further deposition. Figure 3.3 shows that the reflectivity of the nickel upon deposition is similar to that of the simulation in that the intensity first decreases then increases as Ni film thickens. There is a deviation at the start because the simulation considered the deposited film to be continuous at the start and have the optical properties bulk Ni. For a sputtered film, these assumptions are not true, since the Ni film is not continuous in the first few nanometers. The dotted line in the figure show a simulation that has been offset 1.5 nm to show that the intensity rise matches the simulation after the first few nanometers. Figure 3.4 shows a similar reflectivity as the previous deposition in figure 3.3, with the exception that deposition was stopped at 7 nm. For this sample, the monitoring was continued for 2 hours at room temperature with the sputter gas removed after the deposition was complete. The inset of figure 3.4 show the reflectivity of the sample for this two hour period. The increase in intensity is due to restructuring in the sputtered film to an equilibrium state. While the TRDR curves from deposition fit quite naturally into the theoretical optical constructs of how our system should behave, the TRDR signals from the films during dewetting required further analysis.

3.5.2 During Dewetting

An example of the TRDR curves obtained during dewetting for different thicknesses of Ni films is shown in figure 3.5. The dynamics of these TRDR curves

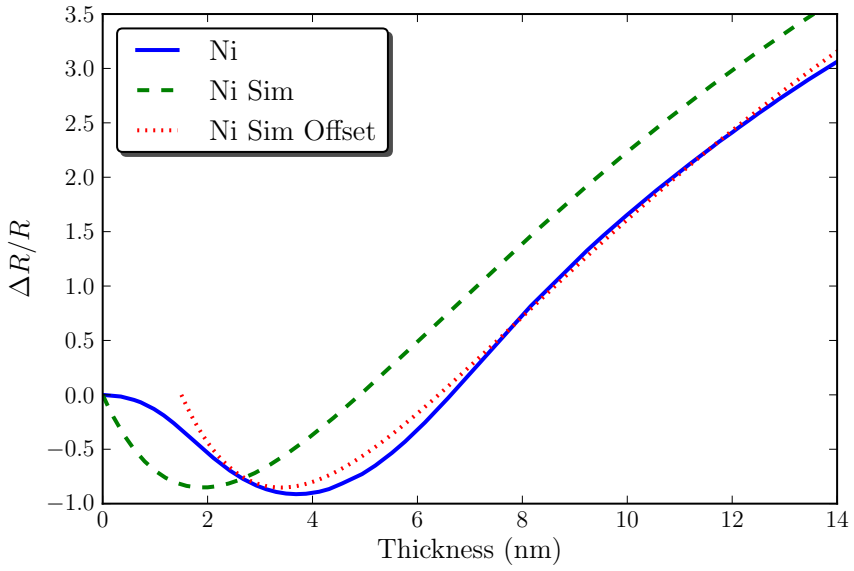

Figure 3.3: A plot of TRDR during a nickel deposition compared to a simulated reflectivity of adding nickel to an SiO_2 layer on Si. The offset is moved 1.5 nm thicker to show the similar slope of the increasing reflectivity.

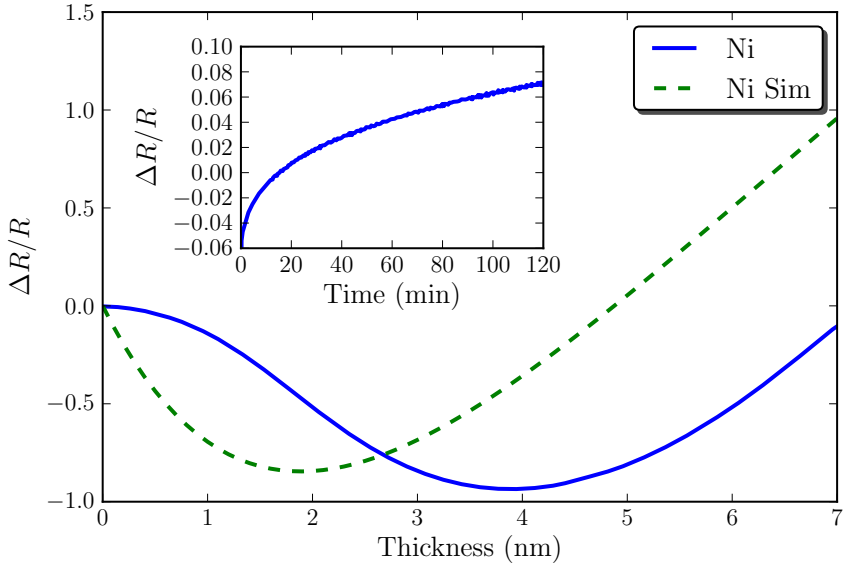

Figure 3.4: A plot of TRDR during a nickel deposition to 7 nm. Inset shows the reflectivity increase after the deposition.

are due to changes in the reflectivity and transmission of the laser light in the Ni film. The curves features, such as reflectivity maxima and minima, relate to certain states of the dewetting thin film. The features of these curves were reproducible, thanks to the sputtering base pressures, to within ± 10 s sample to sample.

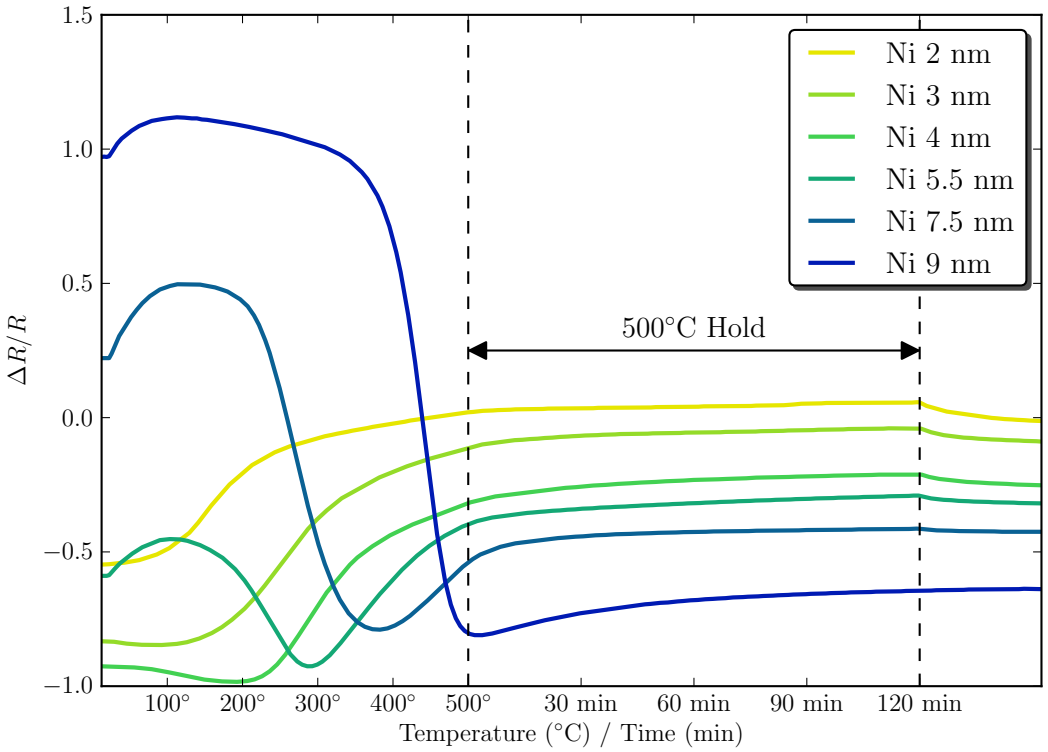

Figure 3.5: A plot of TRDR responses of various Ni film thicknesses on 124 nm SiO_2 samples on Si during a 5°C min^{-1} temperature ramp and annealing 2 hours.

To analyze the states of dewetting on different parts of the curves, 7 nm films were deposited and subsequently annealed to different temperatures and annealing times. Figure 3.6 shows a representative TRDR dewetting curve with labels showing the temperatures/times at which samples were cooled. After these samples were cooled to room temperature and removed from the system, their surface morphologies were measured with AFM. The AFM height

maps seen in figure 3.7 correspond in sample number to the point on the TRDR curve in figure 3.6.

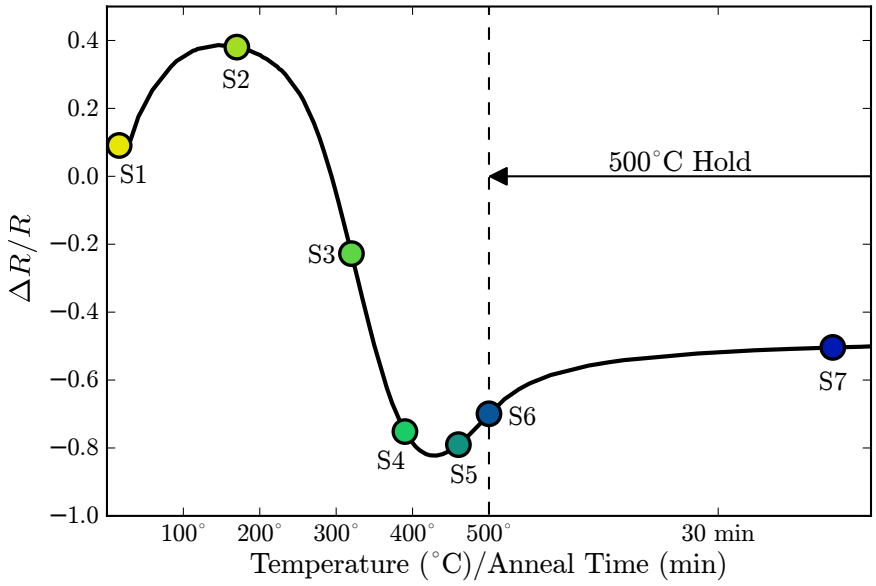

Figure 3.6: A plot of TRDR during annealing of a 7 nm Ni film. The labelled points indicate the parts of the curve where samples were removed from the system and analyzed using AFM.

Sample S1 shows the as-deposited state of the film after the slight surface modifications that are apparent from the reflectivity increase seen in the figure 3.4. The intensity of the reflection then increases with temperature to about 150°C near sample S2. Analyzing figure 3.7 S1 and S2 we see an increase in grain size from 14 ± 2 nm to 20 ± 2 nm. From S2 to S4 figure 3.7 show hole nucleation and growth, which corresponds to a decrease in reflectivity on the TRDR curve. As seen in other works on dewtting Ni, this hole nucleation and growth results from thermal grooving [23]. As the holes grow, the film becomes a network of islands connected by only small necks of Ni. The necks form where two holes grow to meet one another. The minima of the TRDR curve from S4 – S5 shows the passing of the percolation limit, where the necks of Ni pinch off and the film is no longer interconnected. Samples S5 – S7 show separate

islands of Ni on a flat SiO_2 substrate. At this point, the particles coarsen due to Ostwald ripening where large particles become larger at the expense of smaller particles or Smoluchowski ripening, where particles coalesce [29]. As the islands grow in size and thickness, decreasing in number, the TRDR curve shows a slight increase in reflectivity.

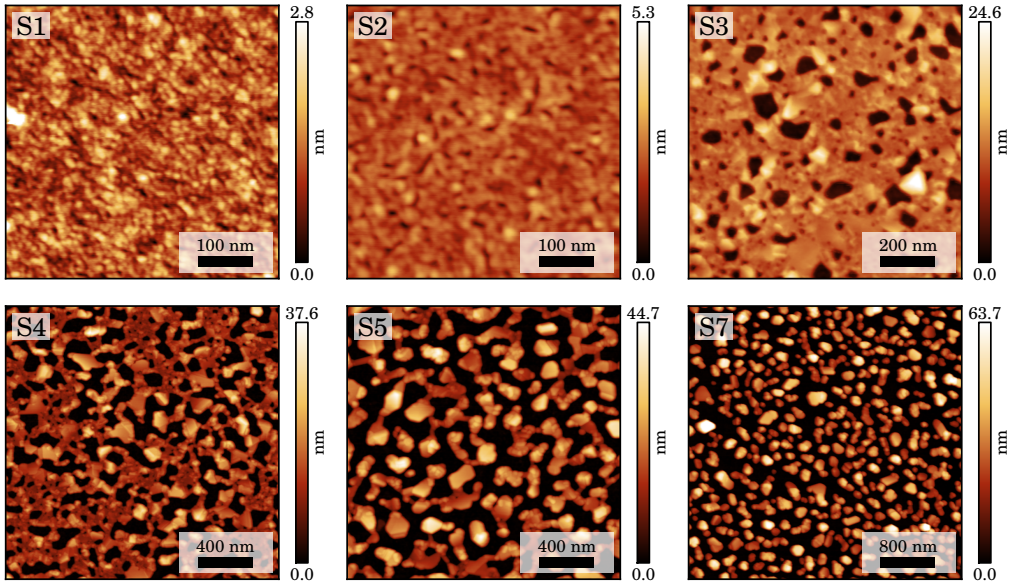

Figure 3.7: AFM height maps of 7 nm dewet Ni films stopped at different points during the anneal. Sample numbers correspond to the points on the curve in figure 3.6.

Attempts were made to use the characteristic matrix approach to model the TRDR curves seen in the dewetting experiments, but special optical constants were needed for the Ni particle film. Effective media theory can find optical constants for particle vacuum films, such as the Ni found in its dewett state [30], but it doesn't apply to the interconnected geometries seen in the AFM height maps. Finite-difference time-domain modelling was used with the AFM height maps to see the reflectivity of the samples directly.

3.6 Finite-Difference Time-Domain Modelling

Finite-difference time-domain (FDTD) modelling uses Maxwell's equations in a Finite-difference form, described by Yee in 1966 [31], to solve for the electric and magnetic field vectors at points on a defined grid. The modelling system is time dependant so the points on the grids are solved sequentially for the electric field then magnetic field. This technique allows for broadband sources allowing for multiple frequencies of light to be studied in one simulation.

The FDTD simulations were performed using commercial software (Lumerical Solutions, Inc.). The samples were setup with the same spacings and orientations as the experimental setup. Since the surface information in the AFM height maps used contained fine details, a small grid was used over that area. The simulations were computationally intensive because of the number of points required to accurately model the fields on the AFM data.

The transmission of the nickel film increased as the area fraction of uncovered SiO_2 increased from sample S3 – S7. This transmission seemed to increase less than expected from the fraction of uncovered SiO_2, due to extra scattering as the Ni particle spacing approaches the wavelength of the light. From this transmission information, one would expect that the TRDR curve from a dewet sample would continue to decrease as the film dewets and never experience a minima as seen in experiments.

As seen in figure 3.8 (a), the reflectivity of the FDTD simulations did produce a result similar to that from experiment (see figure 3.6). The reflectivity decreases to a minima and then increases as the dewetting occurs. The values differ from the experimental TRDR curves because the FDTD simulation still uses the bulk optical values and the internal mircostructure is not accounted for. Figure 3.8 (b) shows the intensity of the reflected wave packets resultant from the incident Gaussian wave packet. The first peak represents the

reflection from the Ni/vacuum interface and the second is from the Si/SiO_2 interface. As the dewetting progress from S3 – S7, the first reflection decreases and the second reflection increases. This is a result of increasing transmission due to opening holes in the Ni film. When the two peaks approach the same value and they are out of phase, then the reflectivity can decrease. The changes in the peak intensities for samples S5 – S7 are slight, but from the inset in 3.8 (b) it can be seen that the peak spacing or Δt is decreasing. This time delay results in phase shift in the two beams, allowing the reflectivity to reach minima and increase. The first reflection shifts to the left, sooner in time, because the nickel particles grow taller as dewetting progresses (see figure 3.7. The taller particles decease the path length taken by the light reflected on the Ni surface. The shift in the second peak is also to the left, sooner in time. This shift is the result of the transmitted light passing though the opening in the Ni film. The light passing through the Ni is slower than light in vacuum so as more oxide surface is exposed, the time delay decreases. This effect is compounded by the decreasing transmission through the Ni particles as their height increases as the result of exposing more oxide.

The FDTD simulations show that the decreasing reflectivity during the dewetting process is a result of increasing transmission and decreasing reflection in the Ni film. This is a result of more oxide being exposed. The curve minima is at film state where there is a critical amount of oxide exposed resulting in phase shift between the two reflected beams, since more of the light is transmitted through the vacuum and oxide only, avoiding the slower Ni. Even though the minima is observed for many thicknesses, it is not expected that the critical exposed oxide is the same for all thicknesses. For more detail on the FDTD modelling, please see the published work [32].

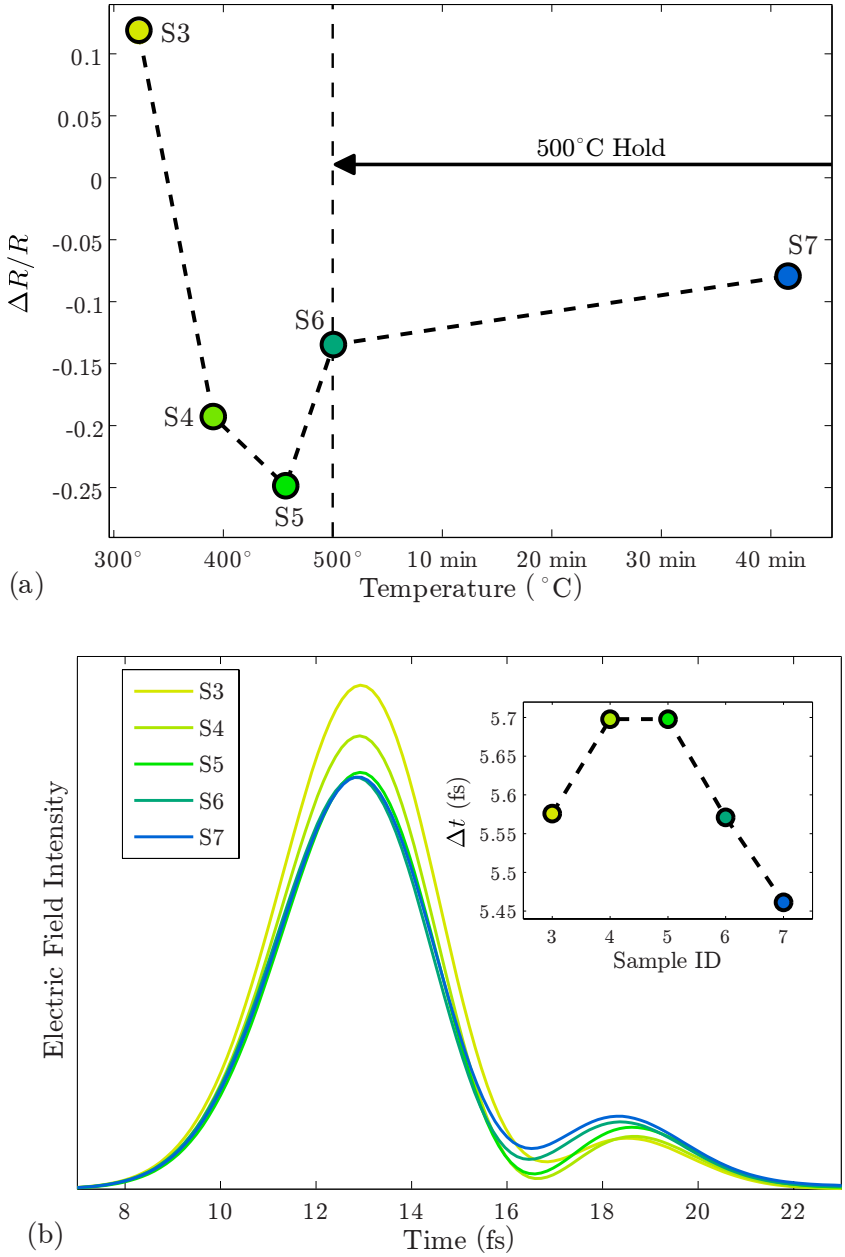

Figure 3.8: Results of the FDTD simulations. (a) show the simulated reflectivity of samples S3 – S7. (b) shows the intensity of the reflected beams and their delay times. Adapted from Luber *et al.* [32].

3.7 Mechanisms of Dewetting

After gaining a better understanding of the TRDR curves seen during dewetting from FDTD modelling and confirming that the features on the curves correspond to a physical state of dewetting in the film, such as dewet fraction, the curves can be used to uncover the mechanisms behind the dewetting process. Since the minima of the TRDR curves correspond to a physical state, the minima can be used as a marker in kinetic analysis of the dewetting film.

3.7.1 Activation Energies

Since the dewetting process is thermally driven and the minima of the TRDR curve corresponds to a repeatable state during dewetting, the time to reach that state can be found by:

$$\tau = A \exp\left(\frac{\Delta E}{k_b T_0}\right) \tag{3.7.1}$$

where A is proportionality constant, k_b is the Boltzmann constant, T_0 is the heating rate dependant characteristic temperature of that state and ΔE is the activation energy. For samples of the same thickness, the TRDR curves for multiple heating rates, 1.0 to 15.0°C min^{-1}, were collected. The time and temperature of the minima were compared to find the activation energy. These are the activation energies of the rate limiting step at the point of the dewetting process that corresponds to the minima. The results of these experiments are found in figure 3.9. Activation energies of 0.31±0.04 and 0.59±0.06 eV were calculated for a Ni thickness of 4 and 7.5 nm respectively. The Kissinger-Akahira-Sunose method is also often applied to dewetting to find activation energies. This analysis gives similar energies of 0.33±0.04 and 0.58±0.06 eV. Kissinger-Akahira-Sunose analysis wasn't used for the case of dewetting since it was derived for phase changes and dewetting is only a change of surface morphology.

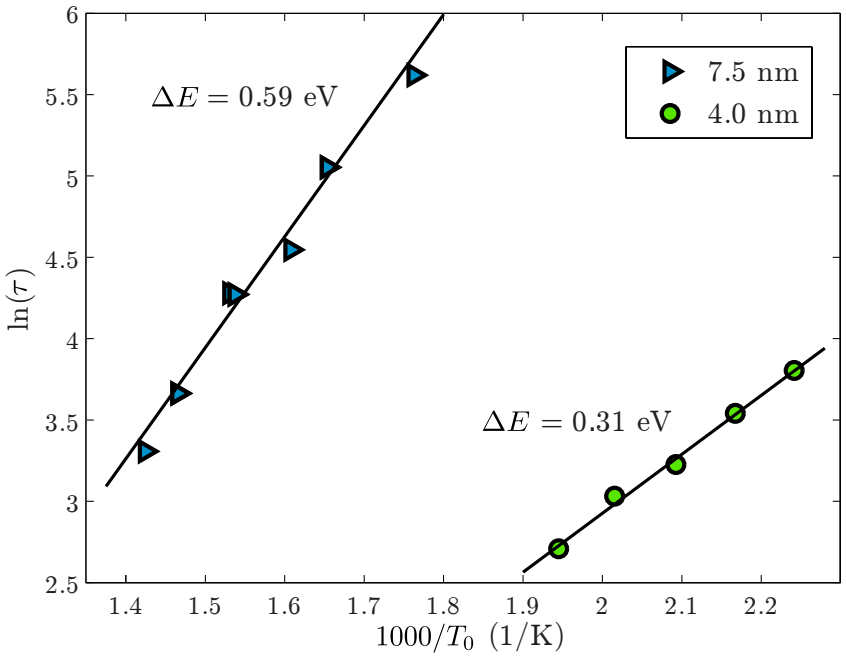

Figure 3.9: The time-temperature pairs of the TRDR curve minima for heating rates from 1.0 to 15.0°C min^{-1}. Activation energies of 0.31±0.04 and 0.59±0.06 eV for 4 and 7.5 nm films respectively were calculated from equation 3.7.1. Adapted from Luber *et al.* [32].

3.7.2 Grain Growth

It is easy to see that the activation energies found for the minima of the 7.5 and 4 nm films represent different rate limiting mechanism. To analyze the state of the dewetting 4 nm film, an AFM time study was performed. The results of this study can be seen in figure 3.10. For the 4nm film, the percolation limit seems to fall between samples A2 and A3, whereas the film minima is before sample A1. The AFM height map for sample A1 shows the film at a stage where the first holes are only beginning to form. The rate limiting step measured by TRDR indicates the process that is limiting the rate of change in the reflectivity. Since the small infrequent holes in the film have little affect on the reflectivity, a process for grain growth may be the rate limiting step.

In fact, similar activation energies have been measured for grain growth in metal films. For grain growth in a Ni film evaporated on mica, an activation energy of 0.25 eV was measured [33]. This measurement was performed through direct observation by TEM, with annealing temperatures from 90 to 420°C. This value agrees with 0.31 eV found for 4 nm Ni, and the deviation could result of differences in deposition or substrates. Through similar TEM studies of grain growth in thin films, activation energies for Au 0.14 eV [34], Cu 0.36 eV [35] and Ag 0.274 eV [36] were measured. These low energy barriers for grain growth in thin films are attributed to additional driving forces from interface [37] or surface [38] energy minimization especially in high aspect ratio thin films or from the high defect density found in deposited thin films [35, 39].

3.7.3 Hole Nucleation and Growth

The higher activation energy of 0.59±0.06 eV for the 7.5 nm minima should be at or near the percolation limit similar to the 7 nm film studied earlier. At

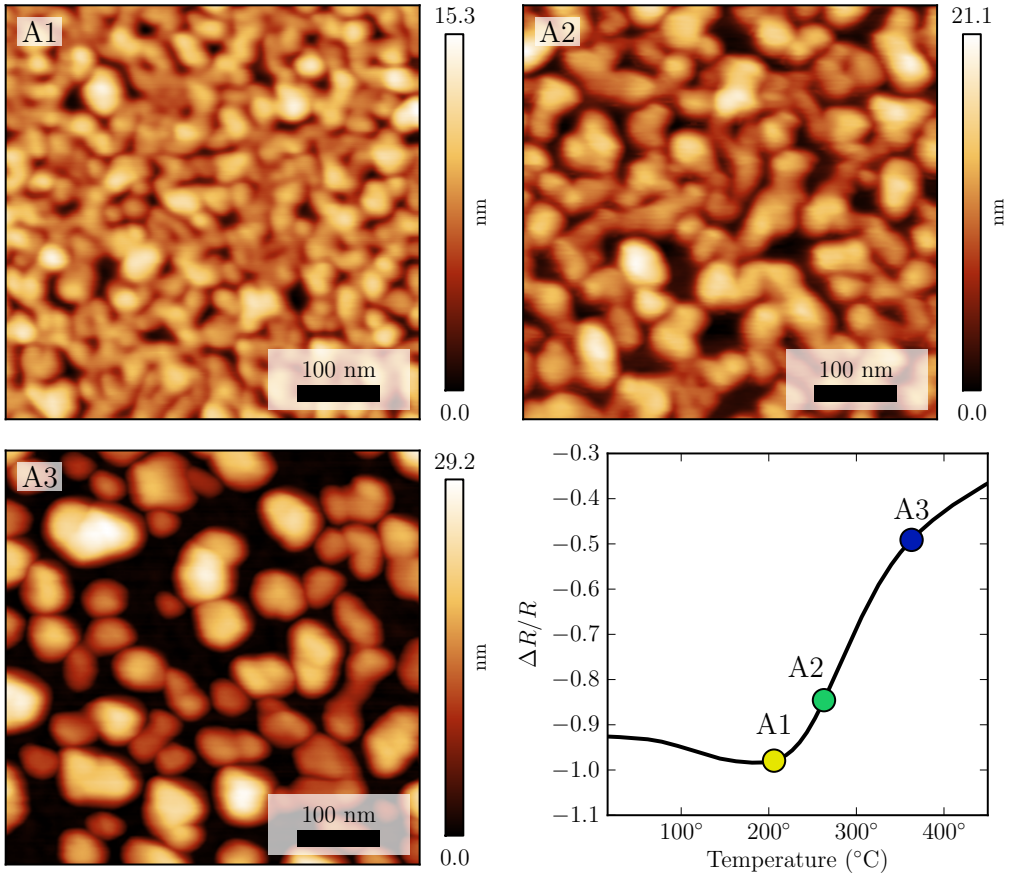

Figure 3.10: AFM height maps of 4 nm dewet Ni films stopped at different points during the anneal. Sample numbers correspond to the points on the curve inset in the figure.

this period of dewetting, the reflectivity is most affected by the hole growth. As more oxide is exposed, the time delay between the two beams is decreased and the reflectivity increases. The activation barrier must be part of the hole growth process. In hole growth, the film thins in some regions and thickens in others. The possible activation barriers would result from thinning of the film by moving from the oxide, atomic transport on the surface and film thickening by grain growth.

From S3 – S5 in figure 3.6 significant thickening occurs. In order to thicken a single crystal particle of metal, a new crystal plane must nucleate on the existing plane. However, the barrier for forming a stable nucleus on a particle $\geqslant 1$ nm in diameter is almost insurmountable [40]. This barrier is much higher than the measured activation energy. However, the particles seen at this stage of the dewetting process are not single crystalline, but have many grains. McCarthy and Brown looked at the coalescence of (111) oriented fcc metal particles and found that the nucleation barrier could be overcome by step flow at the interface between the particles [41]. With this nucleation mechanism, it was found that the coalescence is limited by surface diffusion. X-ray diffraction shows that the sputtered films in this study are highly oriented in the (111) direction. Therefore, the process shown by McCarthy and Brown likely occurs in the films observed this study and film thickening is not rate limiting.

The thinning of the films occurs at the edges of the holes in the film. This hole edge retracts due to curvature induced surface diffusion where the larger curvature is on the hole edge [26]. This process is also limited by surface diffusion. This leaves mass transport of Ni via surface diffusion as the possible rate limiting step. In fact, the activation energy for surface self-diffusion on (111) planes of Ni was measured to be 0.65 ± 0.1 eV [42]. This value agrees well with the value of 0.59 ± 0.06 eV found in this study. This evidence suggests the dewetting of a Ni film near its percolation limit is limited by surface diffusion along the (111) plane of Ni.

4

CrFeNi as a Carbon Nanotube Catalyst

4.1 Motivation

This chapter describes the result of the metal catalyst design experiments performed. Since this catalyst was designed to run in a large commercial CNT reactor, special considerations where made. In chapter 1, the role of the catalyst in CNT growth was discussed. The catalyst must be a template for the nanotubes and should have good carbon solubility. Also, the catalyst particle must be stable against coarsening, since CNT growth may terminate if the growth particle changes in size. Most large commercial reactors have very slow ramp rates [43], where the catalyst films must endure a long anneal

before reaching growth temperatures. Therefore, the thermal stability of the catalyst particle is an important consideration.

4.2 Alloy Composition

Carbon solubility is an important attribute of the catalyst material both for the disassociation of the feed gas and transport of the carbon atoms to the tube growth sites. Ni and Co both have carbon solubilities of >0.5 atomic percent for temperatures above 700°C. Fe has only <0.1 atomic percent carbon solubility in its bcc alpha phase, but in the fcc gamma phase, Fe has solubility of >3 atomic percent. However, the gamma phase does not form until temperatures above 740°C in the presence of carbon, and the phase change in pure iron occurs at 912°C. This limits the growth of CNT on Fe catalyst to recipes with temperatures usually >800°C. At these elevated temperatures the carbon feed gas decomposes to form amorphous carbon more readily, and terminates the growth [1, 44, 45].

4.2.1 Fe-Ni Alloy

Fe grows the tallest and the highest quality of tubes compared to Ni and Co because of its high carbon solubility in the gamma phase [46]. The Fe–Ni binary phase diagram (see figure 4.1 [47]) shows that, by adding Ni to Fe, the stability of the γ-Fe phase increases allowing it to form at lower temperatures [48]. Unfortunately, the Fe–Ni catalyst produced a low density forest of tubes that did not produce a vertical height of more than 2 µm.

To see why the Fe–Ni alloys performed poorly, dewetting experiments were performed similar to the Ni dewetting in chapter 3. The films were deposited to a thickness of 5 nm to allow better measurement in the AFM. The deposited

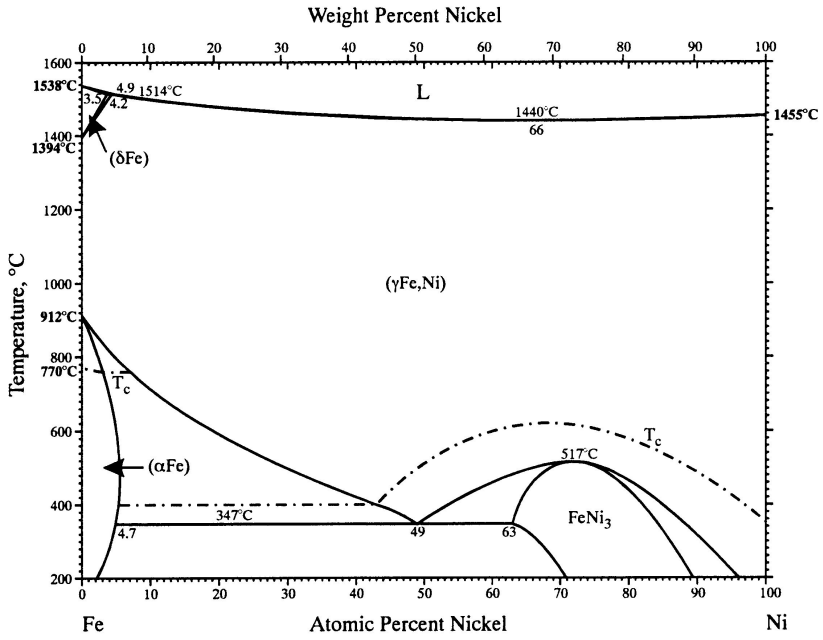

Figure 4.1: Fe-Ni binary phase diagram [47].

samples were heated with a 10°C min^{-1} ramp to 500°C, where they were annealed for two hours. Figure 4.2 shows the AFM height maps measured after the samples were removed. It can be seen in figure 4.2 (b)–(d) that the alloy catalyst exhibits a much lower density of particles and larger average particle size than their constituent pure elements in figure 4.2 (a) and (e). From chapter 3, it was seen that the distribution of the dewet catalyst particles was affected by the grain size during hole nucleation. The grains in the film continue to grow in size as the temperature increases until grain growth is pinned by nucleating holes in the film.

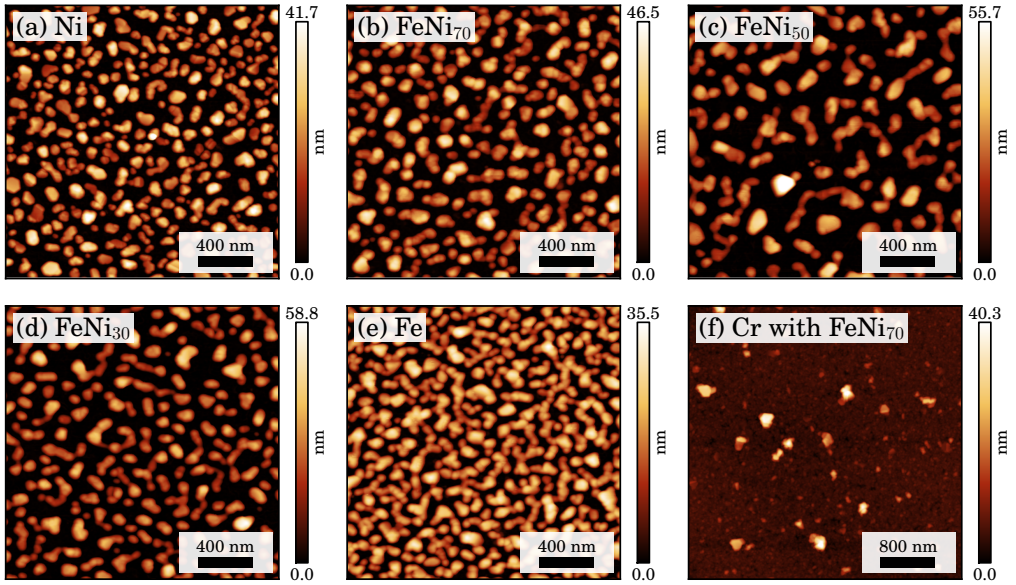

Figure 4.2: (a)–(e) AFM height maps of dewet 5 nm FeNi films at various compositions. (f) Height map of 2.5 nm of Cr with $Fe_{70}Ni_{30}$ that was deposited as a bi-layer structure then annealed.

The TRDR data seen in figure 4.3 shows that the pure Ni film restructures to its dewet state quickly. As more Fe is added, the kinetics of the surface reconstruction slow, requiring higher temperatures to increase the surface mobility of adatoms. The pure Fe film is not even completely separated into islands

after the ramp and anneal as seen in figure 4.2 (e). The TRDR also shows that there is significant grain growth in all but the Ni sample, where the grain growth is stopped short by hole nucleation.

The dewetting of the $Fe_{50}Ni_{50}$ sample is anomalous in both the final particle distribution seen in the AFM height maps and in the TRDR since it overlaps with the $Fe_{70}Ni_{30}$ reflectivity curve. The reason for this result may be because of its high deposition rate due to the co-sputtering technique [49]. The deposition curve for the $Fe_{50}Ni_{50}$ actually shows a decrease in reflectivity which indicates that the state of the film is changing likely due to a decrease of conductivity. In chapter 3, there was an increase in the reflectivity curves of the Ni films after deposition because of increased conductivity of the films due to grain growth. The decrease after deposition in the $Fe_{50}Ni_{50}$ film may be because of oxidization of the film after the deposition. The film with the fastest sputter rate would have the fewest atoms that come in contact with oxygen while travelling to the film, or on the deposition surface [49, 50]. This is supported by the fact that the other more slowly deposited films have no change in reflected intensity after deposition. Those films would already be in equilibrium with the amount of oxygen in the system so no change would occur. Oxidation of the $Fe_{50}Ni_{50}$ could explain the large particle spacing seen in the dewet film as well. The sample would only oxidize on the exposed surface of the film and the rest of the film would have less oxygen content than the slowly deposited films. This sample would have a greater grain boundary mobility that would allow for increased grain growth resulting in fewer grains and larger spacings in the final dewet distribution of particles.

The effect of the oxides on the kinetics of dewetting and its final particle distribution is very important in this study. Since Fe oxide is more stable, the deposition base pressure used was not adequate to produce an oxide free Fe film like the Ni films of chapter 3. This is one of the reasons for the reduced mobility seen in the dewetting kinetics of the Fe film. Another reason may be

that Fe interacts more strongly with the SiO_2 than the Ni, since Fe forms a more stable oxide [51].

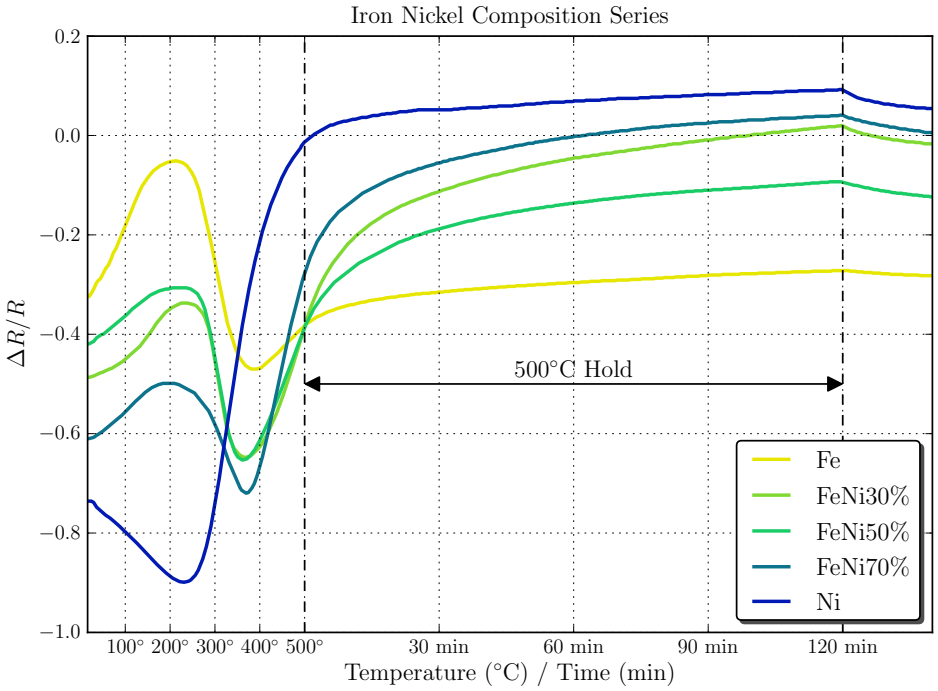

Figure 4.3: TRDR data taken during the dewetting anneal of the 5 nm FeNi films at various compositions shown in figure 4.2 (a)–(e).

4.2.2 Cr-Fe-Ni Alloy

The addition of a Cr underlayer seemed to enhance the growth of the CNT films giving them greater density and therefore greater height [43, 52]. Cr shows little catalytic activity toward CNT growth [46]. Since Cr forms an even more stable oxide than Fe [53, 54], it was used as an addition to make the catalyst more stable against coarsening because of high affinity to the SiO_2. This is shown in figure 4.2 (f) which shows the height map after dewetting a 5 nm $Fe_{70}Ni_{30}$ film on a 2.5 nm underlayer of Cr. Note that the Cr underlayer

does not dewet the surface of the oxide. The surface grooves grow but holes in the film don't grow due to the strong interactions of Cr to the SiO_2 substrate. Also note that the catalyst does not completely mix with the Cr but still dewets on top of the complete underlayer.

To find the best composition of Fe-Ni film to use for CNT growth, a study was performed with 1 nm samples of Fe-Ni at different compositions with a 1 nm Cr underlayer. The height of the VACNT film was measured after growth by SEM. The results, seen in figure 4.4, indicate that the $Fe_{70}Ni_{30}$ composition grows the tallest forest. This result agrees well with work by Yang *et al.* where a Fe–Ni alloy at a composition of $Fe_{66}Ni_{34}$ grew the greatest amount of CNTs by weight [48]. The ternary phase information shown in figure 4.4 for 800°C (not 750°C, but there is little change in this region from 650–800°C) indicates that $Fe_{70}Ni_{30}$ is the highest composition of iron in which a fcc γFe,Ni phase forms. Beyond this, there is not enough Ni to stabilize the γFe and the less catalytic σ(Cr,Fe) phase is in majority.

4.3 VACNT Growth

The previous alloy composition series used bi-layers of 1 nm Cr and 1 nm Fe-Ni and found that $Fe_{70}Ni_{30}$ with an underlayer of Cr grew the highest film. This series of experiments uses the same bi-layer catalyst found previously, $Fe_{70}Ni_{30}$, and tries to enhance the film by changing various catalyst deposition parameters. Figure 4.5 (a) shows the uniform, ∼25 µm tall VACNT film grown by the bi-layer catalyst. In addition to this bi-layer structure, the catalyst was sputtered as a single co-deposition with the compositional equivalent of the bi-layer, $Cr_{50}Fe_{35}Ni_{15}$. The CNT film grown on the $Cr_{50}Fe_{35}Ni_{15}$ grew taller then the bi-layer catalyst to a height of ∼45 µm (see figure 4.5 (c)). Compare this growth to that of a 2 nm $Fe_{70}Ni_{30}$ catalyst without Cr seen in figure 4.5 (e). This film is not consistent in height across the sample and is ∼2.5 µm in

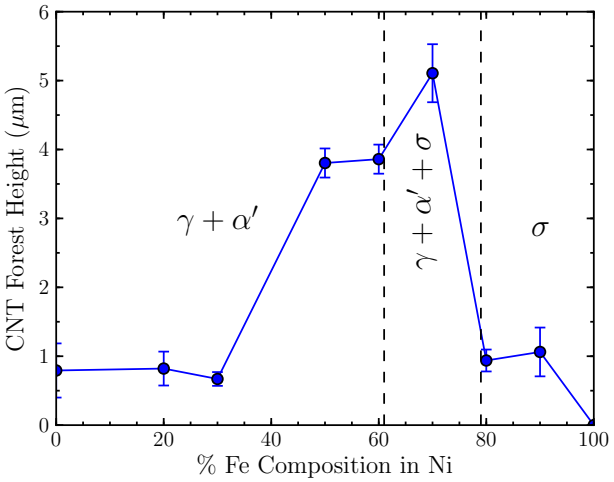

Figure 4.4: CNT forest height vs. atomic % Fe composition in Ni films deposited 1 nm thick with 1 nm Cr underlayer. The corresponding phase information from the Cr-Fe-Ni ternary phase diagram at 800°C is shown in background [47].

height. The final sample tried was a 1 nm $Cr_{50}Fe_{35}Ni_{15}$ co-sputtered catalyst which was only able to produce a few CNTs along with carbon filaments (see figure 4.5 (g)).

Annealing *in situ* after sputtering was performed to see the effects of dewetting the catalyst prior to CVD CNT growth. The catalysts samples were ramped at 10 °C per min to 750 °C under vacuum ($< 1 \times 10^{-8}$ Torr) and held for 15 min before cooling. Other than the *in situ* anneal to pre-dewet the catalyst, the same preparation was used as the previous samples. The right hand column of figure 4.5 shows the growth result of the *in situ* dewet samples next to the left hand as-deposited samples. The only significant differences between the two columns are in the bi-layer catalyst and the 1 nm $Cr_{50}Fe_{35}Ni_{15}$ co-sputtered catalyst. The bi-layer catalyst shows a significant decrease in forest height to just over 2.5 µm. The density of the forest still seems quite high but the growth kinetics seem to have slowed. The 1 nm $Cr_{50}Fe_{35}Ni_{15}$ co-sputtered catalyst, on the other hand, experienced enhanced growth from the *in situ* dewetting process, with a VACNT film height of ∼30 µm. This height is near that of the 2 nm $Cr_{50}Fe_{35}Ni_{15}$ co-sputtered catalyst.

4.4 Dewetting

To understand the effect of Cr in the $Cr_{50}Fe_{35}Ni_{15}$ alloy catalyst, TEM samples were prepared with the *in situ* dewet catalysts used in the previous section. To ensure electron transparency, the TEM samples were deposited and annealed on 20 nm SiO_2 windows, instead of Si wafers with thermally grown $Si0_2$ as used previously. Figure 4.6 (a) and (b) shows the 2 nm $Cr_{50}Fe_{35}Ni_{15}$ co-sputtered catalyst and the 2 nm $Fe_{70}Ni_{30}$ catalyst respectively after an in-situ vacuum anneal in the sputter system. The difference in particle size is negligible. This result was anomalous since it was thought that the particle sizes in the $Fe_{70}Ni_{30}$ catalyst would be large given its relatively poor growth performance(see figure

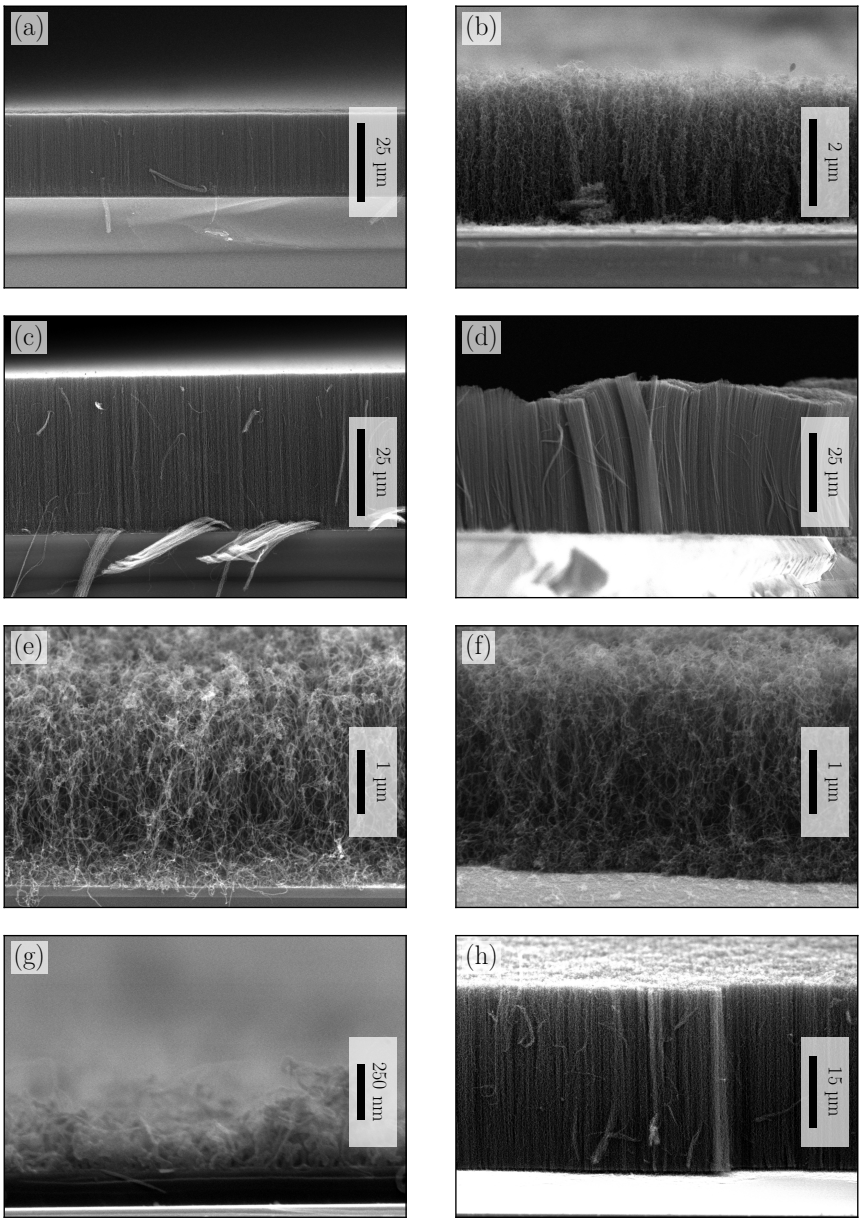

Figure 4.5: SEM micrographs of CNT films resultant from growth on different catalysts. Samples in the left column are from growth on as-deposited catalyst. The right column samples were dewet *in situ* after deposition. (a) and (b) show growth from 1 nm Cr and 1 nm $Fe_{70}Ni_{30}$ bi-layer catalyst. (c) and (d) Similarly for 2 nm $Cr_{50}Fe_{35}Ni_{15}$. (e) and (f) Similarly for 2 nm $Fe_{70}Ni_{30}$ catalyst. (g) and (h) Similarly for 1 nm $Cr_{50}Fe_{35}Ni_{15}$ catalyst.

4.5 (c) and (e)).

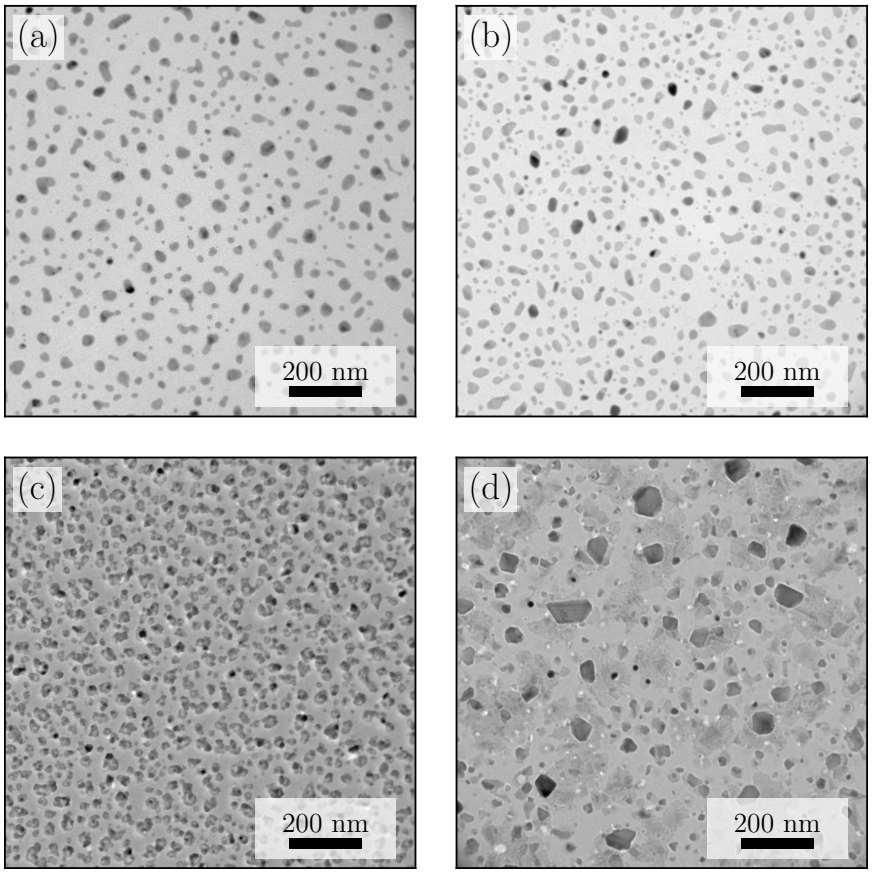

Figure 4.6: TEM micrographs of 2nm thick films dewet at 750°C. (a) and (b) $Cr_{50}Fe_{35}Ni_{15}$ and $Fe_{70}Ni_{30}$ respectively, annealed in-situ. (c) and (d) $Cr_{50}Fe_{35}Ni_{15}$ and $Fe_{70}Ni_{30}$ respectively, annealed in-situ, then annealed in the CVD furnace.

The dewetting environment of the CVD furnace is significantly different from that of the deposition vacuum chamber. To truly compare the TEM samples to the CNT growth, the TEM samples imaged in figure 4.6 (a) and (b) were placed through the CVD process without carbonizing gas. The results of this reactor run can be seen in figure 4.6 (c) and (d). It can be easily seen that the particles in the $Cr_{50}Fe_{35}Ni_{15}$ in figure 4.6 (c) are much smaller than those of the $Fe_{70}Ni_{30}$ catalyst in figure 4.6 (d). Both of these sample have a thin layer

of what may be amorphous carbon contamination, or a result of oxidization of catalyst material after the removal from the furnace at 400°C. Disregarding this contamination, the *in situ* dewet $Cr_{50}Fe_{35}Ni_{15}$ sample shows little particle size increase after the furnace run. This would result in a VACNT film like the one, seen in figure 4.5 (d) formed from a similarly prepared sample. The $Fe_{70}Ni_{30}$ catalyst underwent Oswald ripening in the CVD reactor where a significant increase in particle size is seen [15]. This state would result in a film growth like the one seen in figure 4.5 (e) again, from a similarly prepared sample, where the particles small enough to grow are less densely distributed and prone to size changes leading to early growth termination [13–15].

4.4.1 Effects of Oxidization

This section will discuss the state of the catalyst while dewetting during the anneal step of the CVD reactor. For additional insights, the diffraction rings from the TEM samples are used to probe the state of the catalyst particles. Figure 4.7 shows a diffraction pattern from an as-deposited 2 nm $Cr_{50}Fe_{35}Ni_{15}$ thin film. This diffraction pattern indicates the state of a catalyst film before entry into the CVD reactor. Not much can be said of this diffraction since the as-deposited grains are so small, but this is the only film tested where the Cr_2O_3 in the catalyst can be detected. There may also be metallic Fe, Cr or $FeNi_3$, but unfortunately there is not enough evidence to support this. After exposing such a thin metal film to atmosphere, it is unlikely that any pure metals are still present.

Electron diffraction profiles for three *in situ* dewet samples are shown in figure 4.8. Figure 4.8 (a) shows 2 nm $Fe_{70}Ni_{30}$ catalyst where phases of $FeNi_3$ and α-Fe can be seen. There is also some indications of Ni or Fe oxide similar to figure 2.6 in this profile. Figure 4.8 (b) shows 1 nm Cr and 1 nm $Fe_{70}Ni_{30}$ bi-layer catalyst. In this profile, phases of $FeNi_3$ and α-Fe can still be seen as well

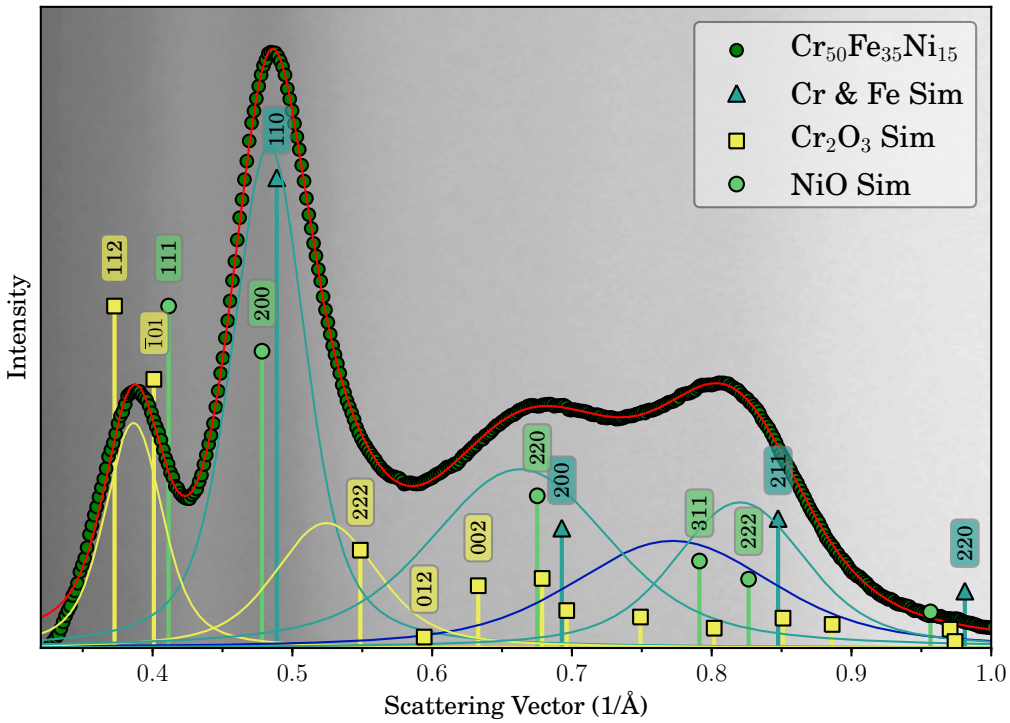

Figure 4.7: A profile of an electron diffraction ring pattern from an as-deposited 2 nm $Cr_{50}Fe_{35}Ni_{15}$ film (green circles). The solid lines represent peak fitting where the red line is the resultant fit and the other lines correspond to the colour of the peak markers from the diffraction simulation.

as a Cr phase, however the α-Fe and the Cr simulations are nearly identical with the Cr shifted $\sim$0.004 Å^{-1} to the left. It is therefore unknown whether Cr or Fe is present. The bcc (110) peak intensity is stronger relative to the other peaks in the profile, than the bcc (110) peak in the 2 nm $Fe_{70}Ni_{30}$ profile. This indicates there is more bcc phase in the 1 nm Cr and 1 nm $Fe_{70}Ni_{30}$ bi-layer catalyst because of the addition of Cr. There may also be a small amount of γ' ($CrNi_2$) phase. The diffraction profile of the 2 nm $Cr_{50}Fe_{35}Ni_{15}$ catalyst shown in figure 4.8 (c) is similar to the 1 nm Cr and 1 nm $Fe_{70}Ni_{30}$ bi-layer catalyst except the features seem washed out due to peak broadening. This may indicate that the 2 nm $Cr_{50}Fe_{35}Ni_{15}$ catalyst has a finer grain size.

Figure 4.9 shows the profiles from the two samples that were placed in the CVD reactor after *in situ* dewetting. These profiles are significantly different from the profiles seen in figure 4.8, since the catalyst is heavily oxidized when removed from the CVD reactor. Since a commercial CVD reactor is always kept at elevated temperatures to minimize the cost of ramping up, the samples are removed from the reactor into air at $\sim$400°C. At this temperature in air, oxides readily form in the materials used [55].

The 2 nm $Fe_{70}Ni_{30}$ catalyst, shown in figure 4.9 (b), indicates the presence of Fe_3O_4, Fe_2O_3 and NiO as would be expected. However, 2 nm $Cr_{50}Fe_{35}Ni_{15}$ catalyst, shown in figure 4.9 (a), indicates only Fe_3O_4 and NiO. This is an interesting result since there is no evidence of the corundum Cr_2O_3 structure as would be expected from exposure of a Cr-Fe alloy to air at 400°C [55]. Cr_2O_3 structure would appear the same as the Fe_2O_3 simulation in figure 4.9 (b).

There is a possibility that some Cr is in the spinel Fe_3O_4 structure but it is more likely that the Cr oxidizes upon entry into the reactor and is never reduced. It is important to remember that the catalyst oxides are not active, so the ramp and anneal of the catalyst in the CVD reactor prior to growth is performed in a reducing environment of 10% hydrogen in argon. According

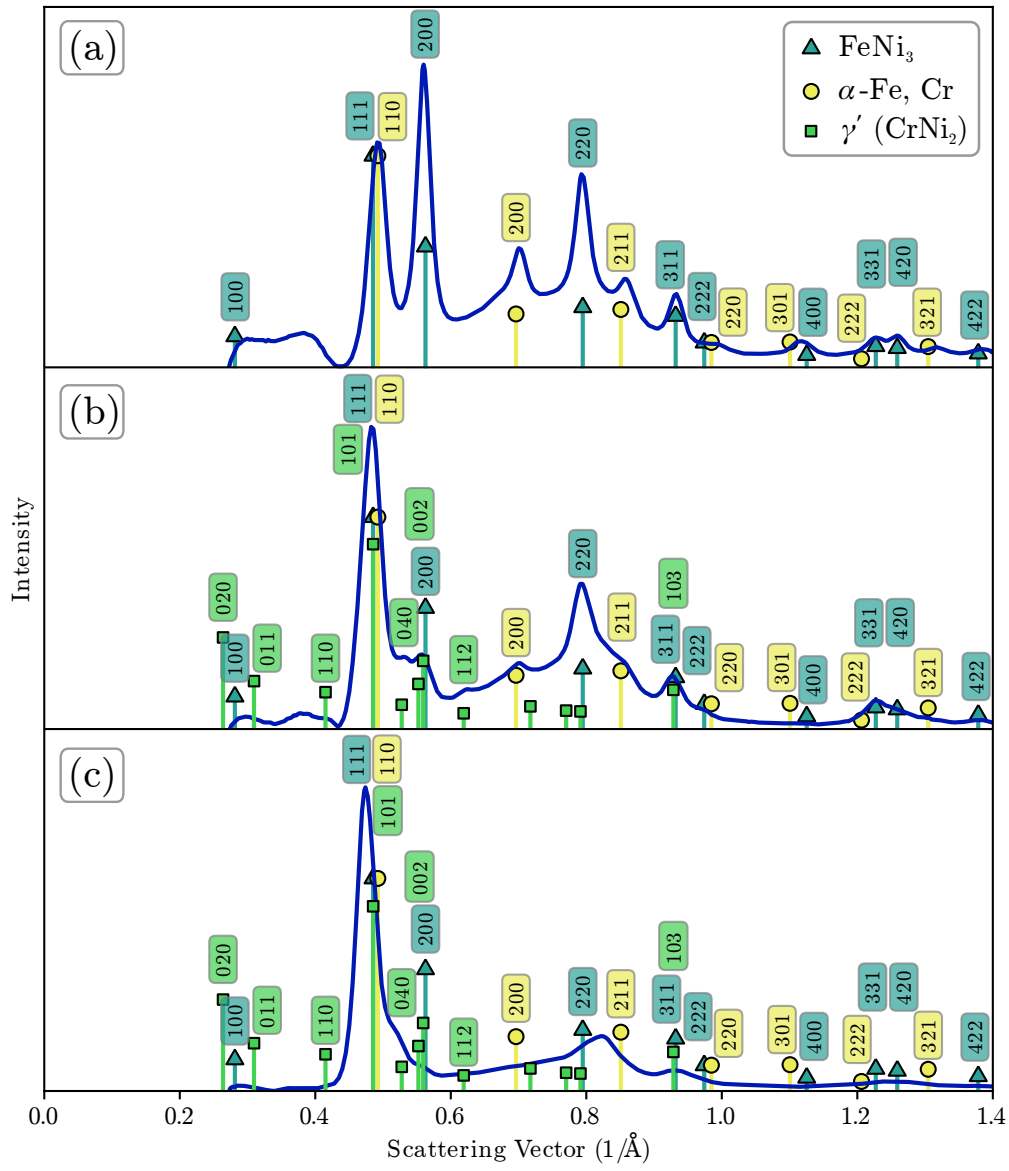

Figure 4.8: Profiles of electron diffraction ring patterns from *in situ* dewet films of (a) 2 nm $Fe_{70}Ni_{30}$ catalyst, (b) 1 nm Cr and 1 nm $Fe_{70}Ni_{30}$ bi-layer catalyst and (c) 2 nm $Cr_{50}Fe_{35}Ni_{15}$ catalyst.

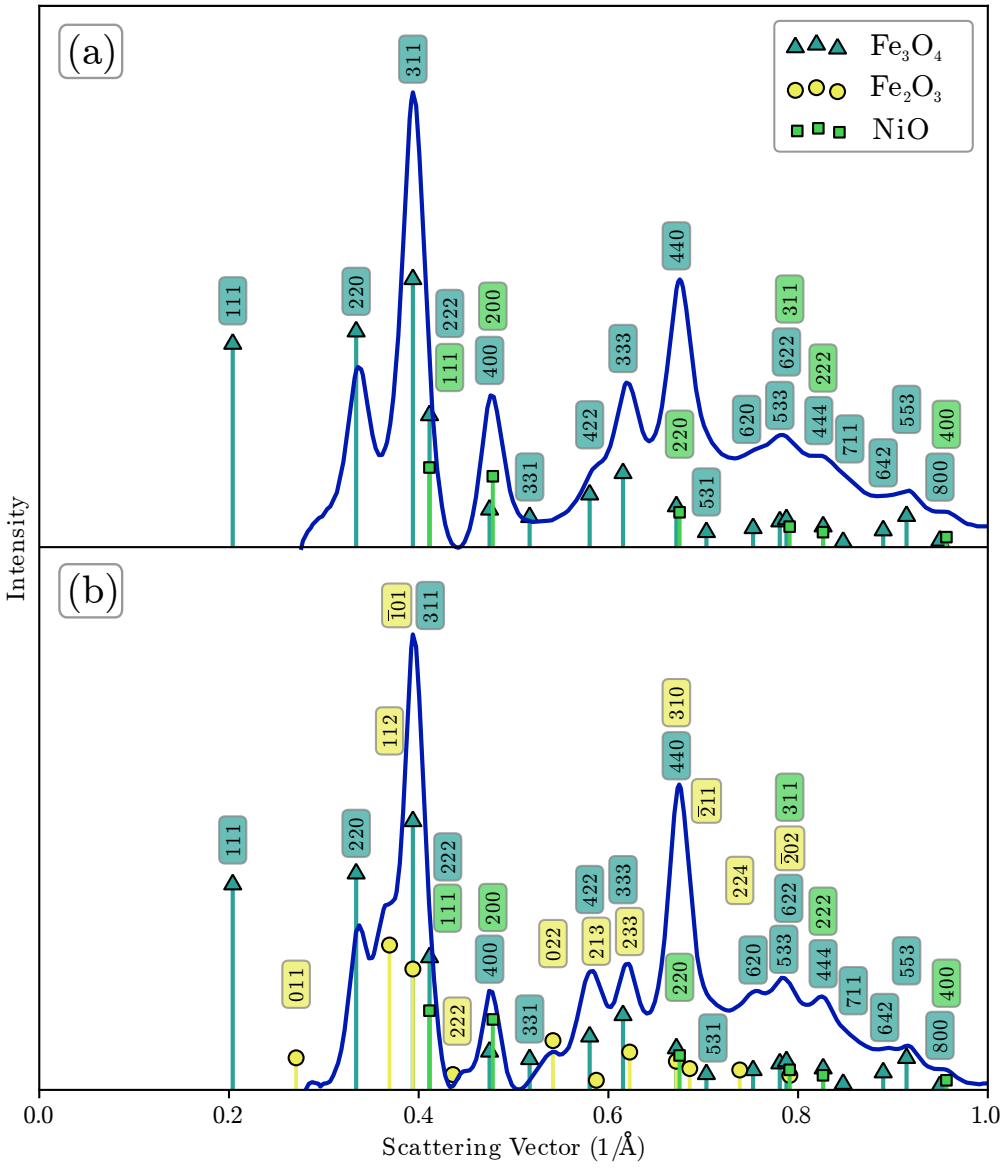

Figure 4.9: Profiles of electron diffraction ring patterns from films of (a) $Cr_{50}Fe_{35}Ni_{15}$ catalyst and (b) 2 nm $Fe_{70}Ni_{30}$ catalyst that were *in situ* dewet and then put through the CVD reactor without carbon containing gas.

to the Ellingham diagram [56], the P_{H_2}/P_{H_2O} ratio needed to reduce Cr at 750°C must be $\gtrsim 10^5$ which would necessitate having <1 ppm of H_2O in the CVD reactor. In order to achieve <1 ppm of H_2O the Ar purge would have to have >6.0 (99.9999%) purity, whereas the argon connected to the CVD reactor is only 4.8 pure. With 4.8 purity, the reducing environment in the CVD has a P_{H_2}/P_{H_2O} ratio of $\lesssim 10^4$, which is insufficient to reduce Cr_2O_3. However, a P_{H_2}/P_{H_2O} ratio of $\lesssim 10^4$ is more than enough to reduce Ni and Fe, which require ratios of $\gtrsim 10^{-2}$ and $\gtrsim 1$ respectively at 750°C. The samples are placed into the reactor in air at 500°C and then the reactor is sealed and purged. This process takes several minutes, therefore, it is likely that all the catalyst is oxidized at this point and only the Ni and Fe oxides are reduced during the anneal [57].

Since oxidized Cr in the sample cannot be reduced, this Cr_2O_3 would stay as small grains in the catalyst at the catalyst interfaces or on the substrate as the Fe oxides around them reduce [58]. Small Cr_2O_3 grains would be difficult to detect through diffraction because of broadening and would not coalesce to form larger grains because of their stability at 750°C. This in turn would also limit the Ostwald ripening process in that adatom mobility on the surface of the particle and the substrate would be reduced.

4.5 CNT Characteristics

To see the results of an effective CNT growth, a TEM sample with 2 nm $Cr_{50}Fe_{35}Ni_{15}$ catalyst was placed in the CVD reactor and the growth time was limited to 30 seconds. The growth was limited so that the VACNT forest would be thin enough to allow for the inspection of the CNT catalyst particles. Before the sample was placed in the TEM apparatus, a part of the VACNT film was scraped away and the oxide window was punctured.

The result of the TEM sample growth is show in figure 4.10. The CNTs grown with the 2 nm $Cr_{50}Fe_{35}Ni_{15}$ catalyst, shown in figure 4.10 (a) and (b), are mostly MWCNT. There are a few that are the right diameter for single walled tubes, but without high resolution TEM, it is difficult to be certain. The diameters range from $\sim$ 3–30 nm with the majority of the tubes between 10–15 nm. Figure 4.10 (c) shows a section of the SiO_2 window where the CNTs are scraped away to reveal the catalyst particles on the window. A darkfield micrograph of the same area is shown in figure 4.10 (d), where the aperture is placed over the (311) ring of Fe_3O_4. This clearly shows catalyst particles still on the window, also no catalyst tipped CNTs were observed. Therefore, the dominant growth orientation for the CNTs is base growth, where the CNTs are grown from catalyst particles adhered to the substrate.

The electron diffraction pattern, shown as the blue curve in figure 4.11, is taken from a CNT covered area. The resulting pattern is heavily influenced by the diffraction of MWCNT, as indicated by the excellent match with the profile from MWCNT diffraction, shown as the yellow curve. The XRD pattern shown [59] matches well to the MWCNT diffraction profiles. The (002) peak is a result of the spacing in the concentric CNTs of the MWCNT, where the spacing of 0.35 nm is near that of the (002) spacings of graphite at 0.34 nm. The catalyst can be seen as Fe_3O_4 because of oxidization of the catalyst on removal from the CVD reactor. This is similar to the pattern of 2 nm $Cr_{50}Fe_{35}Ni_{15}$ catalyst that was placed in the CVD reactor without growth gas, seen in figure 4.9 (a). It is interesting to note that the catalyst did not form a stable carbide as a result of the growth gas since an oxide readily formed on catalyst removal.

4.6 Summary

This study shows that the best performing catalyst layer is 2nm $Cr_{50}Fe_{35}Ni_{15}$, both in the as-deposited and *in situ* dewet samples. The 2nm $Cr_{50}Fe_{35}Ni_{15}$

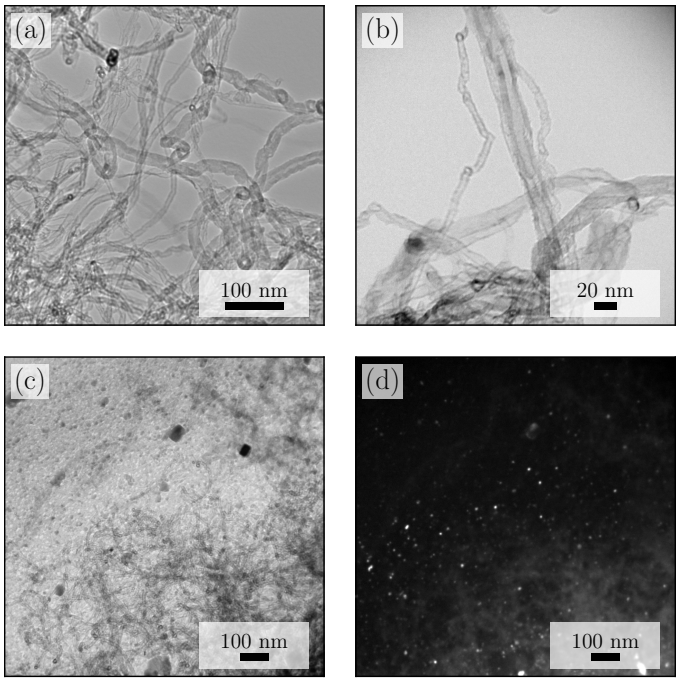

Figure 4.10: TEM micrographs of CNTs grown on 2nm $Cr_{50}Fe_{35}Ni_{15}$. (a) MWCNTs over an opening in the SiO_2 window. (b) A detail of a typical 20 nm MWCNT (c) A section of SiO_2 window where the CNTs have been scraped away revealing the growth particles on the substrate.(d) A darkfield micrograph of (c) on the (311) ring of Fe_3O_4 showing the catalyst particles as bright spots

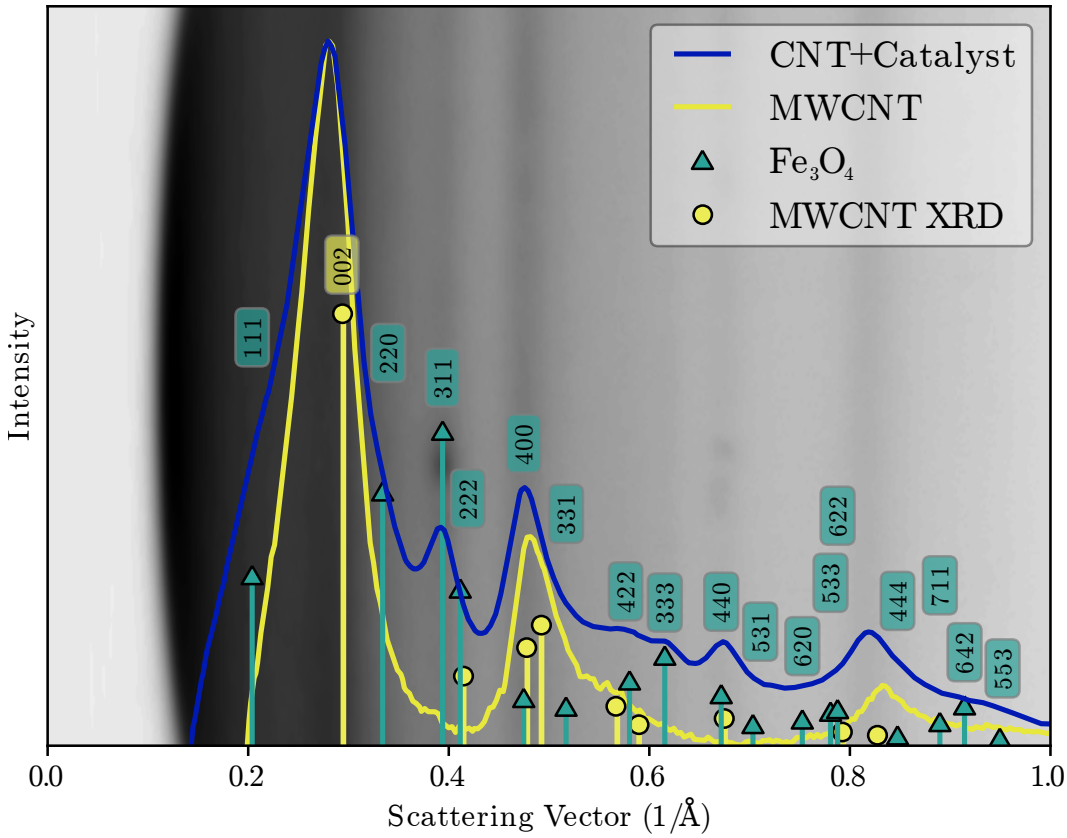

Figure 4.11: Profiles of an electron diffraction ring patterns from an area of the CNT covered 2nm $Cr_{50}Fe_{35}Ni_{15}$ sample, showing diffraction from MWCNTs and Fe_3O_4. The MWCNT XRD, shown for spacing comparison, is taken from Li *et al.* [59].

catalyst can grow VACNT forest of over 45 µm in height because of the phases present at 750°C and its stability against particle coarsening due to Ostwald ripening. It is hypothesized that, this stability is a result of Cr oxide that, unlike Fe and Ni, does not reduce during the temperature ramp and anneal in the reactor. The catalyst forms a VACNT film that is comprised of MWCNT that experience base growth, where the average CNT diameter is ∼12 nm.

5

Conclusions

5.1 Thesis Summary

This work covered the role of the metal catalysts in the growth of VACNT film by CCVD, and looked for ways to improve the stability and functionality of the catalysts. The dynamics of solid state metal thin film dewetting were important since it determined the final state of the catalyst particles used to grow the CNTs, which in turn determined the size and distribution of the VACNT film grown. The stability of the particles against coarsening, once dewet into particles fit for growth, was also a concern, since Ostwald ripening changes the particle sizes during growth and can cause termination.

Chapter 5: Conclusions

The process of solid-state dewetting was studied by looking at the dewetting of Ni films *in situ* after deposition. The dewetting process of Ni was monitored *in situ* using TRDR, and different points of the dewetting process were probed *ex situ* through AFM. This study showed that upon heating of the sample there was a period of grain growth. The activation energy associated with this step was found to be 0.31±0.04 eV. Grain growth was followed by thermal grooving at the grain boundaries. This grooving caused holes to nucleate along grain boundaries. The growth of these holes was mediated by curvature induced surface diffusion of atoms from the hole edge along the Ni surface to thicken the edge of the hole. This step corresponded to an activation energy of 0.59±0.06 eV, which was found to be surface diffusion of adatoms on the (111) surface of Ni. The holes continued to grow until the necks of metal separating the holes retracted and the film became individual islands. The particles still coarsened after this point through Ostwald and Smoluchowski ripening.

After the principles of dewetting were explored, a more applied scenario of dewetting was found in the growth of VACNT films in a commercial sized reactor. A 2 nm thick catalyst of $Cr_{50}Fe_{35}Ni_{15}$ was found to produce the tallest VACNT film at 750°C. The film height was over 45 µm. The composition supported enough fcc γ-Fe phase to have the carbon solubility necessary for a good catalyst. Commercial reactors are held at high temperature and are slow to ramp to temperature, so the catalyst must have stability against particle coarsening. Adding the Cr to the catalyst gave this stability since the Cr oxides that formed before the CVD process were not reduced in the reducing environment prepared to reduce Ni and Fe oxides before growth. The Cr oxide, therefore, acted as a barrier to coarsening of the film. The CNTs grown by the 2 nm $Cr_{50}Fe_{35}Ni_{15}$ catalyst were MWCNTs with an average diameter of ∼12 nm. The catalyst was found to adhere to the substrate during growth exhibiting the base growth orientation of the VLS growth mechanism.

References

[1] K. Hata, D. N. Futaba, K. Mizuno, T. Namai, M. Yumura, and S. Iijima. Water-assisted highly efficient synthesis of impurity-free single-walled carbon nanotubes. *Science*, 306(5700):1362–4, 2004.

[2] S. Iijima. Helical microtubules of graphitic carbon. *Nature*, 354(6348):56–58, 1991.

[3] H. W. Kroto, J. R. Heath, S. C. O'Brien, R. F. Curl, and R. E. Smalley. C_{60}: Buckminsterfullerene. *Nature*, 318(6042):162–163, 1985.

[4] T. W. Odom, J. L. Huang, P. Kim, and C. M. Lieber. Atomic structure and electronic properties of single-walled carbon nanotubes. *Nature*, 391(6662):62–64, 1998.

[5] J. W. G. Wildöer, L. C. Venema, A. G. Rinzler, R. E. Smalley, and C. Dekker. Electronic structure of atomically resolved carbon nanotubes. *Nature*, 391(6662):59–62, 1998.

[6] F. Kreupl, A. P. Graham, G. S. Duesberg, W. Steinhögl, M. Liebau, E. Unger, and W. Hönlein. Carbon nanotubes in interconnect applications. *Microelectronic Engineering*, 64(1-4):399–408, 2002.

[7] R. S. Wagner and W. C. Ellis. Vapor-liquid-solid mechanism of single crystal growth. *Applied Physics Letters*, 4(5):89–90, 1964.

[8] R. T. K. Baker, P. S. Harris, R. B. Thomas, and R. J. Waite. Formation of filamentous carbon from iron, cobalt and chromium catalyzed decomposition of acetylene. *Journal of Catalysis*, 30(1):86–95, 1973.

[9] H. Kanzow and A. Ding. Formation mechanism of single-wall carbon nanotubes

on liquid-metal particles. *Physical Review B*, 60(15):11180, 1999.

[10] F. Ding, A. Rosén, and K. Bolton. The role of the catalytic particle temperature gradient for SWNT growth from small particles. *Chemical Physics Letters*, 393(4-6):309–313, 2004.

[11] S. Hofmann, R. Sharma, C. Ducati, G. Du, C. Mattevi, C. Cepek, M. Cantoro, S. Pisana, A. Parvez, F. Cervantes-Sodi, et al. In situ observations of catalyst dynamics during surface-bound carbon nanotube nucleation. *Nano Letters*, 7(3):602–608, 2007.

[12] F. Ding, A. Rosén, and K. Bolton. Molecular dynamics study of the catalyst particle size dependence on carbon nanotube growth. *J Chem Phys*, 121(6):2775–9, 2004.

[13] M. Bedewy, E. R. Meshot, H. Guo, E. A. Verploegen, W. Lu, and A. J. Hart. Collective mechanism for the evolution and self-termination of vertically aligned carbon nanotube growth. *The Journal of Physical Chemistry C*, 113(48):20576–20582, 2009.

[14] K. Hasegawa and S. Noda. Diameter increase in millimeter-tall vertically aligned single-walled carbon nanotubes during growth. *Applied Physics Express*, 3(4):045103, 2010.

[15] S. M. Kim, C. L. Pint, P. B. Amama, D. N. Zakharov, R. H. Hauge, B. Maruyama, and E. A. Stach. Evolution in catalyst morphology leads to carbon nanotube growth termination. *The Journal of Physical Chemistry Letters*, 1(6):918, 2010.

[16] Y. Y. Wei, G. Eres, V. I. Merkulov, and D. H. Lowndes. Effect of catalyst film thickness on carbon nanotube growth by selective area chemical vapor deposition. *Applied Physics Letters*, 78:1394–1396, 2001.

[17] Y. Li, W. Kim, Y. Zhang, M. Rolandi, D. Wang, and H. Dai. Growth of single-walled carbon nanotubes from discrete catalytic nanoparticles of various sizes. *The Journal of Physical Chemistry B*, 105(46):11424–11431, 2001.

[18] Y.-G. Baek, S. Honda, T. Ikuno, S. Ohkura, M. Katayama, T. Hirao, and K. Oura. Formation of graphite layers during carbon nanotubes growth. *Japanese Journal of Applied Physics*, 42(Part 1, No. 2A):579, 2003.

[19] L. C. Qin. CVD synthesis of carbon nanotubes. *Journal of Materials Science Letters*, 16(6):457–459, 1997.

[20] G. Binnig, C. F. Quate, and C. Gerber. Atomic force microscope. *Physical review letters*, 56(9):930–933, 1986.

[21] M. Wojdyr. *Fityk*: a general-purpose peak fitting program. *Journal of Applied Crystallography*, 43(5 Part 1):1126–1128, 2010.

[22] R. Saxena, M. J. Frederick, G. Ramanath, W. N. Gill, and J. L. Plawsky. Kinetics of voiding and agglomeration of copper nanolayers on silica. *Physical Review B*, 72(11):115425, 2005.

[23] J. Petersen and S. G. Mayr. Dewetting of Ni and NiAg solid thin films and formation of nanowires on ripple patterned substrates. *Journal of Applied Physics*, 103(2):023520, 2008.

[24] S. J. Randolph, J. D. Fowlkes, A. V. Melechko, K. L. Klein, H. M. Meyer III, M. L. Simpson, and P. D. Rack. Controlling thin film structure for the dewetting of catalyst nanoparticle arrays for subsequent carbon nanofiber growth. *Nanotechnology*, 18(46):465304, 2007.

[25] D. T. Danielson, D. K. Sparacin, J. Michel, and L. C. Kimerling. Surface-energy-driven dewetting theory of silicon-on-insulator agglomeration. *Journal Of Applied Physics*, 100:083507, 2006.

[26] E. Jiran and C. V. Thompson. Capillary instabilities in thin, continuous films. *Thin Solid Films*, 208(1):23–28, 1992.

[27] W. W. Mullins. Theory Of Thermal Grooving. *Journal Of Applied Physics*, 28:333–339, 1957.

[28] S. Larouche and L. Martinu. OpenFilters: open-source software for the design,

optimization, and synthesis of optical filters. *Applied optics*, 47(13):219, 2008.

[29] P. A. Thiel, M. Shen, D. J. Liu, and J. W. Evans. Coarsening of two-dimensional nanoclusters on metal surfaces. *The Journal of Physical Chemistry C*, 113(13):5047–5067, 2009.

[30] M. Gilliot, A. En Naciri, L. Johann, J. Stoquert, J. J. Grob, and D. Muller. Optical anisotropy of shaped oriented cobalt nanoparticles by generalized spectroscopic ellipsometry. *Physical Review B*, 76(4), 2007.

[31] K. Yee. Numerical solution of initial boundary value problems involving Maxwell's equations in isotropic media. *Antennas and Propagation, IEEE Transactions on*, 14(3):302–307, 1966.

[32] E. J. Luber, B. C. Olsen, C. Ophus, and D. Mitlin. Solid-state dewetting mechanisms of ultrathin Ni films revealed by combining *in situ* time resolved differential reflectometry monitoring and atomic force microscopy. *Physical Review B*, 82(8):085407, 2010.

[33] V. Starỳ and K. Šefčik. Electrical resistivity and structure of thin nickel films–effect of annealing. *Vacuum*, 31(8-9):345–349, 1981.

[34] N. Mancini and E. Rimini. Annealing of polycrystalline Au and Au-Ag thin films. *Surface Science*, 22(2):357–364, 1970.

[35] S. Simões, R. Calinas, M. T. Vieira, M. F. Vieira, and P. J. Ferreira. In situ TEM study of grain growth in nanocrystalline copper thin films. *Nanotechnology*, 21(14):145701, 2010.

[36] R. Dannenberg, E. A. Stach, J. R. Groza, and B. J. Dresser. In-situ TEM observations of abnormal grain growth, coarsening, and substrate de-wetting in nanocrystalline Ag thin films. *Thin Solid Films*, 370(1-2):54–62, 2000.

[37] E. A. Holm and S. M. Foiles. How grain growth stops: a mechanism for grain-growth stagnation in pure materials. *Science*, 328(5982):1138–41, 2010.

[38] C. V. Thompson. Grain growth in polycrystalline thin films of semiconductors.

Interface Science, 6(1):85–93, 1998.

[39] C. Detavernier, S. Rossnagel, C. Noyan, S. Guha, C. Cabral, and C. Lavoie. Thermodynamics and kinetics of room-temperature microstructural evolution in copper films. *Journal of Applied Physics*, 94(5):2874, 2003.

[40] W. W. Mullins and G. S. Rohrer. Nucleation barrier for volume-conserving shape changes of faceted crystals. *Journal of the American Ceramic Society*, 83(1):214–16, 2000.

[41] D. McCarthy and S. Brown. Evolution of neck radius and relaxation of coalescing nanoparticles. *Physical Review B*, 80(6), 2009.

[42] M. Ondrejcek, M. Rajappan, W. Swiech, and C. P. Flynn. Step fluctuation studies of surface diffusion and step stiffness for the Ni(111) surface. *Physical Review B*, 73(3), 2006.

[43] L. Dai, P. Wang, and K. Bosnick. Large-scale production and metrology of vertically aligned carbon nanotube films. *Journal of Vacuum Science & Technology A: Vacuum, Surfaces, and Films*, 27:1071, 2009.

[44] S. Helveg, C. López-Cartes, J. Sehested, P. L. Hansen, B. S. Clausen, J. R. Rostrup-Nielsen, F. Abild-Pedersen, and J. K. Nørskov. Atomic-scale imaging of carbon nanofibre growth. *Nature*, 427(6973):426–429, 2004.

[45] D. Futaba, K. Hata, T. Yamada, K. Mizuno, M. Yumura, and S. Iijima. Kinetics of water-assisted single-walled carbon nanotube synthesis revealed by a time-evolution analysis. *Physical Review Letters*, 95(5), 2005.

[46] C. P. Deck and K. Vecchio. Prediction of carbon nanotube growth success by the analysis of carbon–catalyst binary phase diagrams. *Carbon*, 44(2):267, 2006.

[47] H. Baker, editor. *ASM Handbook Volume 3: Alloy Phase Diagrams*. ASM International, 1992.

[48] Y. Yang, Z. Hu, Y. J. Tian, Y. N. Lü, X. Z. Wang, and Y. Chen. High-yield

production of quasi-aligned carbon nanotubes by catalytic decomposition of benzene. *Nanotechnology*, 14(7):733, 2003.

[49] T. T. Bardin, J. G. Pronkoz, R. C. Budhani, J. S. Lin, and R. F. Bunshah. The effects of oxygen concentration in sputter-deposited molybdenum films. *Thin Solid Films*, 165(1):243–247, 1988.

[50] T. Imura, K. Ushita, and A. Hiraki. Spontaneous inclusion of oxygen in sputter-deposited amorphous silicon during and after fabrication. *Japanese Journal of Applied Physics*, 19(2):65–68, 1980.

[51] Y. Wang, Z. Luo, B. Li, P. S. Ho, Z. Yao, L. Shi, E. N. Bryan, and R. J. Nemanich. Comparison study of catalyst nanoparticle formation and carbon nanotube growth: Support effect. *Journal of Applied Physics*, 101(12):124310, 2007.

[52] B. Chen and P. Wu. Aligned carbon nanotubes by catalytic decomposition of C_2H_2 over Ni–Cr alloy. *Carbon*, 43(15):3172, 2005.

[53] J. E. Holliday and R. P. Frankenthal. Characterization of passivating films on Fe-Cr alloys by soft x-ray spectroscopy. *Journal of the Electrochemical Society*, 119:1190, 1972.

[54] R. L. Park, J. E. Houston, and D. G. Schreiner. Chromium depletion of vacuum annealed stainless steel surfaces. *Journal of Vacuum Science and Technology*, 9(2):1023–1027, 1972.

[55] A. D. Pelton, H. Schmalzried, and J. Sticher. Computer-assisted analysis and calculation of phase diagrams of the Fe–Cr–O, Fe–Ni–O and Cr–Ni–O systems. *Journal of Physics and Chemistry of Solids*, 40(12):1103–1122, 1979.

[56] D. R. Gaskell. *Introduction to the Thermodynamics of Materials*. Taylor & Francis, 4^{th} edition, 2003.

[57] T. Ohmi, Y. Nakagawa, M. Nakamura, A. Ohki, and T. Koyama. Formation of chromium oxide on 316L austenitic stainless steel. *Journal of Vacuum Science*

& Technology A: Vacuum, Surfaces, and Films, 14(4):2505–2510, 1996.

[58] Y. G. Gurevich, I. D. Radomysel'skii, L. F. Barshchevskaya, N. R. Frage, and Y. I. Pozhidaev. Thermodynamic analysis of the reduction of a mixture of iron and chromium oxides by hydrogen. *Soviet Powder Metallurgy and Metal Ceramics*, 14(1):13, 1975.

[59] J. Li, W. Lei, X. Zhang, X. Zhou, Q. Wang, Y. Zhang, and B. Wang. Field emission characteristic of screen-printed carbon nanotube cathode. *Applied Surface Science*, 220(1-4):96–104, 2003.